Magnetization Damping in Microstructured Ferromagnetic Materials

by

Lei Zhang
B.Sc., Tongji University, 2011

A Thesis Submitted in Partial Fulfillment of the
Requirements for the Degree of

MASTER OF SCIENCE

in the Department of Physics and Astronomy

Magnetization Damping in Microstructured Ferromagnetic Materials

by

Lei Zhang
B.Sc., Tongji University, 2011

Supervisory committee

Dr. Byoung-Chul Choi, Supervisor
(Department of Physics and Astronomy)

Dr. Geoffrey. M. Steeves, Departmental Member
(Department of Physics and Astronomy)

Dr. Natia Frank, Outside Member
(Department of Chemistry)

Supervisory committee

Dr. Byoung-Chul Choi, Supervisor
(Department of Physics and Astronomy)

Dr. Geoffrey. M. Steeves, Departmental Member
(Department of Physics and Astronomy)

Dr. Natia Frank, Outside Member
(Department of Chemistry)

ABSTRACT

The magnetization damping properties of square permalloy elements were characterized. These 20 nm-thick permalloy squares were deposited by the electron beam evaporation. Time resolved magneto-optic Kerr effect microscopy (TR-MOKE) was used to measure the magnetization evolution in the sample. By curve fitting in Matlab, I obtained the value of damping constant that is consistent with the reference paper.

A Landau configuration in the square permalloy sample leads to the different trends of the damping constant with external bias field. The damping constant in the bottom domain is found to decrease with increasing bias field while the damping constant in the top domain has been saturated into the minimum value. The decreasing tendency of magnetization precession frequencies is consistent with the Kittel equation modified with an anisotropic energy term.

Additionally, FePt thin films and patterned CoFeB disks were investigated but neither yielded conclusive dynamic data.

Contents

List of Tables

List of Figures

ACKNOWLEDGEMENTS

I would like to sincerely thank:

Prof. Byoung-Chul Choi, for being a knowledgeable and patient supervisor.

Prof. Y.K. Hong, for his support on the sample deposition.

Jonathan Rudge, Joseph Kolthammer and Haitian Xu for their great help and knowledge.

My family and friends for their love.

Chapter 1

Introduction

1.1 Memory devices

The development of memory devices is driven by information technology industry. In the table 1.1, parameters in four major types of memory devices on the market are listed. Depending on the different physics principle, they have different features, which can be mostly gathered within the magnetic memory. For the next-generation magnetic memory devices, we aim for the ultrafast response time below nanosecond and ultrahigh density greater than 1 $Tbit/in^2$. And this magnetic based memory is quite promising to work as the *universal memory*.

	MRAM	SRAM	DRAM	FLASH
Physical	Magnetic	Semiconductor	Semiconductor	Semiconductor
Read speed	Fast	Fastest	Medium	Fast
Write speed	Fast	Fastest	Medium	Low
Non-volatility	Yes	No	No	Yes
Density	Ultrahigh	Medium	High	Medium
Power consumption	Low	Medium	High	Low

Figure 1.1: Table of major memory devices.

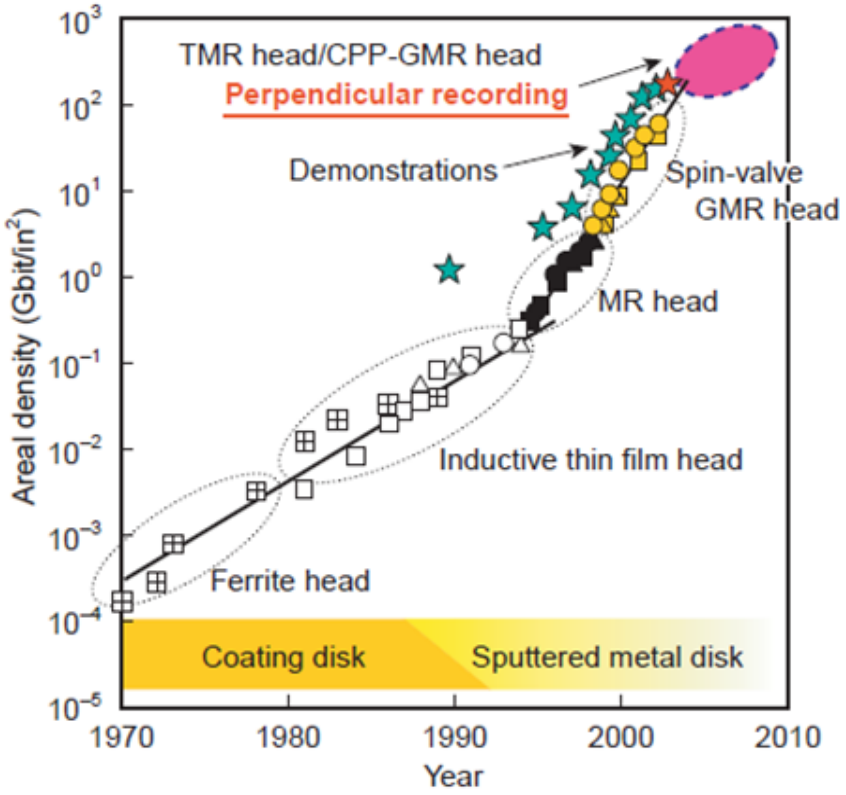

Figure 1.2: Increase in areal density for hard disks over the last 40 years. MR is the magnetoresistance, GMR is the giant MR, TMR is the tunneling MR and CPP is current-perpendicular to plane. Adapted from IBM website [1].

1.2 Magnetic memory devices

Fig. 1.2 shows the significant increase in hard disk areal density achieved over the last forty years. The areal density is defined as the number of memory bits stored per unit area and is generally described in gigabytes per square inch. To obtain the ultrahigh density of memory bits, the high perpendicular magnetic anisotropy (PMA) magnetic materials such as Fe-Pt alloys are chosen. Besides, the advanced fabrication technique such as extreme ultraviolet (EUV) lithography technique, could reduce the scale of these memory unit cell.

Fig. 1.3 provides an example, illustrating how the memory state is related to the material magnetization configuration. The square could be single-layer ferromagnetic material or multilayer structures such as magnetic tunnel junction, MTJ. The schematic of the STT-MRAM (spin-transfer torque magnetic random-access mem-

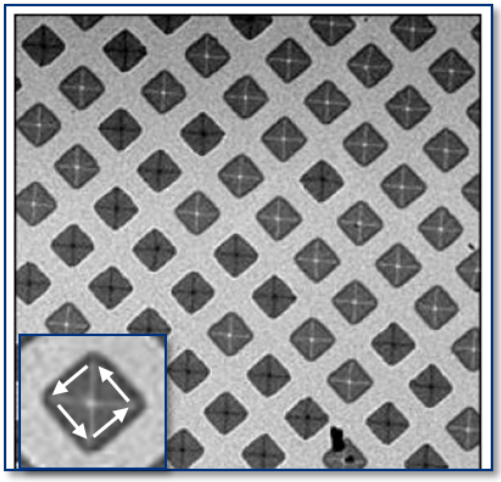

Figure 1.3: Nanoscale building blocks of magnetic storage media. Each block can be used as a memory bit and the color contrast (black and white) stands for the binary state, 0 and 1 [2].

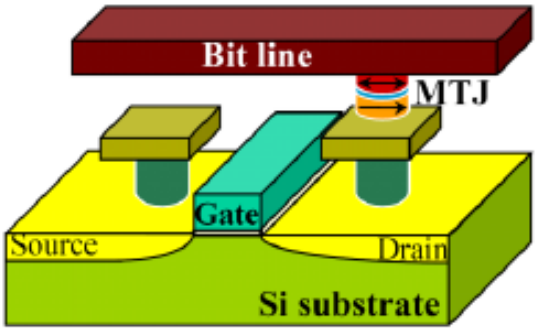

Figure 1.4: Schematic diagram of STT-MRAM. The basic structure of a MTJ unit contains three parts, pinning layer (orange), space layer (blue) and free layer (red). [3]

ory) element is shown in the Fig. 1.4. The relative magnetization orientation of the free layer and pinning layer, i.e., in parallel or in anti-parallel, results in different magnetoresistance of the MTJ element which can be detected by the read circuit.

The underlying principle of switching the magnetic state is the spin transfer torque effect [3], and the switching current depends on several parameters such as damping constant α, saturation magnetization M_s, effective anisotropy field H_k and magnetic

material volume V,

$$I_{switch} = \alpha \frac{\gamma}{\mu_B g} M_s H_k V. \tag{1.1}$$

Generally, the effective damping constant α refers to the rate at which the magnetization relaxes to its equilibrium position. The large damping constant will give rise to the short response time of memory writing. However, on the other hand, as shown in the equation 1.1, the writing current is linearly proportional to the damping parameter. This is the reason why the damping behavior in the magnetic material is a critical determinant for application of the memory devices.

Chapter 2

Micromagnetism

This chapter briefly describes the precession and damping phenomena in the framework of micromagnetism. Micromagnetic theory was first introduced by William Fuller Brown Jr. in 1963. It is now widely used in the numerical simulation to analyze interactions between magnetic moments on sub-micrometre length scales. Based on this semi-classical model, I outline the derivation of the dynamic equation, which covers the phenomenological equation proposed in 1935 by Landau and Lifshitz [4] and includes Gilbert's modification [5].

2.1 Micromagnetic model

2.1.1 Larmor precession

For the free electron, the magnetic dipole moment $\mu_{\mathbf{s}}$ is linearly proportional to the spin angular momentum $\mathbf{S}$,

$$\boldsymbol{\mu} = \gamma_e \mathbf{S} \tag{2.1}$$

Here, $\gamma_e = g_e \mu_B / \hbar$ is the gyromagnetic ratio, μ_B is the Bohr magneton, $\hbar$ is the reduced Planck constant and the Lande factor $g_e \approx 2$.

An external magnetic field produces a torque on the spin angular momentum by $\mathrm{d}\mathbf{S}/\mathrm{d}t = \boldsymbol{\mu} \times \mathbf{H}$. Using (2.1), we have

$$\frac{\mathrm{d}\boldsymbol{\mu}}{\mathrm{d}t} = -\gamma_e \boldsymbol{\mu} \times \mathbf{H}. \tag{2.2}$$

Solving (2.2) gives the Larmor precession frequency, named after Joseph Larmor.

$$f_L = \frac{\gamma_e H}{2\pi}, \tag{2.3}$$

Generally, Larmor precession is the precession of the magnetic moments of electrons, atomic nuclei, and atoms about an external magnetic field H.

2.1.2 The continuum framework

Micromagnetism is a continuum theory to describe the behaviour of the magnetization vector field in micrometer-scale ferromagnetic structures. To use the finite-element model, we have two important assumptions to bridge the scale gap between single-electron Larmor precession and finite-volume cell's average magnetization [6].

A ferromagnetic body with volume V is meshed into finite unit cells $dV_{\mathbf{r}}$, and $\mathbf{r}$ is the position vector, $\mathbf{r} \in V$. Each cell contains N electron's magnetic dipole moment $\mu_{\mathbf{i}}(i = 1, 2...N)$. For the dimension of $dV_{\mathbf{r}}$, we make two assumptions here.

1. It is small enough that all magnetic dipole moments $\mu_{\mathbf{i}}$ in each cell are uniformly aligned. These magnetic moments $\mu_{\mathbf{i}}$ in a unit cell add up as a "macrospin".

2. It is large enough that the macrospin vector distribution is continuous and the difference between adjacent unit cells is small compared with the macrospin magnetization vector.

Now we can define the magnetization vector field $\mathbf{M}(\mathbf{r})$ as the magnetic moment per unit cell volume,

$$\mathbf{M}(\mathbf{r}) = \frac{\sum_{i=1}^{N} \mu_i}{dV_{\mathbf{r}}} \tag{2.4}$$

Substituting (2.4) into (2.2), we get the dynamic equation for magnetization vector field $\mathbf{M}(\mathbf{r})$,

$$\begin{aligned} \frac{1}{\mathrm{d}V_{\mathbf{r}}} \frac{\mathrm{d}\sum_{i=1}^{N} \boldsymbol{\mu}_i}{\mathrm{d}t} &= -\gamma \frac{\sum_{i=1}^{N} \boldsymbol{\mu}_i}{\mathrm{d}V_{\mathbf{r}}} \times \mathbf{H} \\ \Rrightarrow \frac{\partial \mathbf{M}}{\partial t} &= -\gamma \mathbf{M} \times \mathbf{H} \end{aligned} \tag{2.5}$$

2.2 Landau-Lifshitz equation

2.2.1 The effective field

The first dynamic model for the precessional motion of magnetization was proposed by Landau and Lifshitz in 1935. By replacing $\mathbf{H}$ with the effective field $\mathbf{H}_{\text{eff}}$ in (2.5), we arrive at the continuum precession equation,

$$\frac{\partial \mathbf{M}}{\partial t} = -\gamma \mathbf{M} \times \mathbf{H}_{\text{eff}}. \tag{2.6}$$

The equivalent field $\mathbf{H}_{\text{eff}}$ is obtained by minimizing the Gibbs free energy of the magnetic system composed of exchange energy, anisotropy energy, magnetostatic energy and Zeeman energy.

For convenience, we can define a magnetization unit-vector field $\mathbf{m}$, $\mathbf{M} = M_s\mathbf{m}$, where M_s is the saturation magnetization.

First, we write down the first-order variation of Gibbs free energy δG,

$$\begin{aligned} \delta G = -\int_{\Omega} [2\nabla \cdot (A\nabla \mathbf{m}) - \frac{\partial \varepsilon_{\text{an}}}{\partial \mathbf{m}} + \mu_0 M_s \mathbf{H}_m \\ + \mu_0 M_s \mathbf{H}_a] \cdot \delta \mathbf{m} \mathrm{dV} + \int_{\delta\Omega} [2A \frac{\partial \mathbf{m}}{\partial \mathbf{n}} \cdot \delta \mathbf{m}] \mathrm{dS} = 0 \end{aligned} \tag{2.7}$$

where ε_{an} is the anisotropy energy, $\mathbf{H}_m$ is the magnetostatic field, $\mathbf{H}_a$ is the anisotropy magnetic field, $\delta\Omega$ is the unit cell volume and $\mathbf{n}$ is the unit cell surface vector.

Replacing $\delta\mathbf{m}$ in (2.7) by a vector field rotation,

$$\delta \mathbf{m} = \mathbf{m} \times \delta \boldsymbol{\theta} \tag{2.8}$$

which is compatible with the constraint $\mid \mathbf{m} + \delta\mathbf{m} \mid = 1$, or $\mid \mathbf{M} + \delta\mathbf{M} \mid = M_s$. Now we can substitute (2.8) into (2.7) and simplify with $\mathbf{a} \cdot (\mathbf{b} \times \mathbf{c}) = -\mathbf{c} \cdot (\mathbf{b} \times \mathbf{a})$,

$$\begin{aligned} \delta G = \int_{\Omega} \mathbf{m} \times [2\nabla \cdot (A\nabla \mathbf{m}) - \frac{\partial \varepsilon_{\text{an}}}{\partial \mathbf{m}} + \mu_0 M_s \mathbf{H}_m \\ + \mu_0 M_s \mathbf{H}_a] \cdot \delta \boldsymbol{\theta} \mathrm{dV} + \int_{\delta\Omega} [2A \frac{\partial \mathbf{m}}{\partial \mathbf{n}} \times \mathbf{m}] \cdot \delta \boldsymbol{\theta} \mathrm{dS} = 0 \end{aligned} \tag{2.9}$$

Since the elementary rotation $\delta\boldsymbol{\theta}$ is arbitrary, (2.9) can be identically zero only if

$$\mathbf{m} \times [2\nabla \cdot (A\nabla \mathbf{m}) - \frac{\partial \varepsilon_{\text{an}}}{\partial \mathbf{m}} + \mu_0 M_s \mathbf{H}_m + \mu_0 M_s \mathbf{H}_a] = 0$$
$$\text{and} \quad [2A\frac{\partial \mathbf{m}}{\partial \mathbf{n}} \times \mathbf{m}]_{\delta\Omega} = 0. \tag{2.10}$$

Now we can define the terms inside the square brackets in the first equation of (2.10) as $\mathbf{H}_{\text{eff}}$,

$$\mathbf{H}_{\text{eff}} = \frac{2}{\mu_0 M_s}\nabla \cdot (A\nabla \mathbf{m}) - \frac{1}{\mu_0 M_s}\frac{\partial \varepsilon_{\text{an}}}{\partial \mathbf{m}} + \mathbf{H}_m + \mathbf{H}_a \tag{2.11}$$

Therefore the first equation of (2.10) implies that the torque exerted by the effective field is zero in the equilibrium state.

And the second equation can be satisfied only if $\partial \mathbf{m}/\partial \mathbf{n} = 0$. So combining these two conditions, we arrive at Brown's Equations,

$$\mu_0 \mathbf{M} \times \mathbf{H}_{\text{eff}} = 0$$
$$\left.\frac{\partial \mathbf{m}}{\partial \mathbf{n}}\right|_{\delta\Omega} = 0. \tag{2.12}$$

The famous Stoner-Wohlfarth model is an analytic solution to Brown's equations in the specific case of a magnetic body with spheroidal geometry. Generally, we must use numerical techniques to obtain the magnetization distribution to obtain nonuniform magnetization distribution in the equilibrium state of ferromagnetic materials.

2.2.2 Phenomenological dissipation

The second Brown's equation defines the Neumann boundary condition for the partial differential equation (2.6), which implies the energy conservation within the domain.

Nevertheless, in experimental observations, dissipation takes place in the dynamic magnetization process. The microscopic nature of this dissipation is still not well understood. Previous studies suggest that rate-independent mechanisms, including dry friction between domain walls, impurity and crystal dislocation, are responsible for most energy loss.

To this end, Landau and Lifshitz modified (2.6) by introducing a phenomenological

dissipative term,

$$\frac{\partial \mathbf{M}}{\partial t} = -\gamma \mathbf{M} \times \mathbf{H}_{\text{eff}} - \frac{\lambda}{M_s} \mathbf{M} \times (\mathbf{M} \times \mathbf{H}_{\text{eff}}) \tag{2.13}$$

Here, $\lambda > 0$ is a phenomenological material constant. The damping acts as an additional torque that pushes the magnetization in the direction of the effective field.

2.3 Landau-Lifshitz-Gilbert equation

Gilbert proposed a different approach in 1955. The conservative equation (2.6) can be derived from a Lagrangian formulation where the role of the generalized coordinates is played by the components of magnetization vector M_x, M_y and M_z. A viscous force was introduced into this generalized coordinate framework. The components of this viscous force are proportional to the time derivatives of M_x, M_y and M_z. The additional torque term ends up with the form,

$$\frac{\alpha}{M_s} \mathbf{M} \times \frac{\partial \mathbf{M}}{\partial t} \tag{2.14}$$

where $\alpha > 0$ is the Gilbert damping constant for the particular material, with a typical value of $0.001 \sim 0.1$.

$$\frac{\partial \mathbf{M}}{\partial t} = -\gamma \mathbf{M} \times \mathbf{H}_{\text{eff}} + \frac{\alpha}{M_s} \mathbf{M} \times \frac{\partial \mathbf{M}}{\partial t} \tag{2.15}$$

The new precession equation, modified according to Gilbert's work, is generally referred as Landau-Lifshitz-Gilbert equation.

Multiplying both sides of (2.15) by $\mathbf{M}$ and using the vector identity $\mathbf{a} \times (\mathbf{b} \times \mathbf{c}) = \mathbf{b}(\mathbf{a} \cdot \mathbf{c}) - \mathbf{c}(\mathbf{a} \cdot \mathbf{b})$ and $\mathbf{M} \cdot \frac{\partial \mathbf{M}}{\partial t} = 0$, we obtain

$$\mathbf{M} \times \frac{\partial \mathbf{M}}{\partial t} = -\gamma \mathbf{M} \times (\mathbf{M} \times \mathbf{H}_{\text{eff}}) - \alpha M_s \frac{\partial \mathbf{M}}{\partial t} \tag{2.16}$$

Inserting (2.16) back into the second term of (2.15), we have

$$\frac{\partial \mathbf{M}}{\partial t} = -\frac{\gamma}{1+\alpha^2} \mathbf{M} \times \mathbf{H}_{\text{eff}} - \frac{\gamma \alpha}{M_s(1+\alpha^2)} \mathbf{M} \times (\mathbf{M} \times \mathbf{H}_{\text{eff}}) \tag{2.17}$$

Comparing with the modified Landau-Lifshitz(LL) equation (2.13), we can find a relation between the constants,

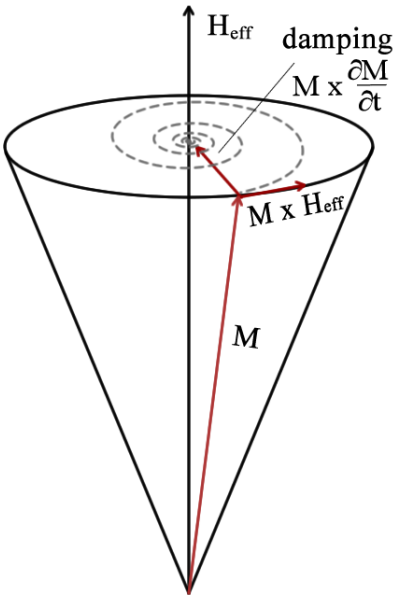

Figure 2.1: Schematic of LLG precession.

$$\gamma_L = \frac{\gamma}{1+\alpha^2},\ \lambda = \frac{\gamma\alpha}{1+\alpha^2} \tag{2.18}$$

P. Podio-Guidugli pointed out that both Landau-Lifshitz and Landau-Lifshitz-Gilbert(LLG) equations belong to the same family of damped gyromagnetic precession equations [7].

Moreover, Kikuchi first studied the limit of infinite damping in the paper *on the minimum of magnetization reversal time* [8], $\lambda \to \infty$ in the modified LL equation (2.13) while $\alpha \to \infty$ in LLG equation (2.15). Respectively, time evolutions of the magnetization in these two equations have the following form:

$$\frac{\partial \mathbf{M}}{\partial t} \to \infty,\quad \frac{\partial \mathbf{M}}{\partial t} \to 0 \tag{2.19}$$

Compared with the infinite change of magnetization in the LL equation, the Landau-Lifshitz-Gilbert equation is more suitable to describe the real magnetization precession in the material.

Chapter 3

Gilbert damping

We have known from Chapter 2 that Gilbert introduced a damping term to the Landau-Lifshitz equation to describe the dissipation phenomenon. This chapter will present more details on the fundamental quantum-mechanical nature of the damping term and introduce several models to calculate the value of damping constant.

For application, tuning the damping parameter will allow us to optimize magnetodynamic properties in the material, such as lowering the switching current and increasing the writing speed of magnetic memory devices.

3.1 Damping classification

To explain the damping mechanism in quantum mechanics, a quasi-particle magnon, is defined as a collective excitation of the electrons' spin in a crystal lattice. In the equivalent wave picture of quantum mechanics, it can be viewed as a quantized spin wave.

As shown in the Fig. 3.1, damping dynamics can be divided into two categories: indirect and direct damping, depending on the direction of energy transfer. If energy is conserved within the magnetic system and redistributed between different magnetic degrees of freedom such as spin wave excitation, the damping is indirect. The direct damping transfers the energy mainly to the lattice.

The direct damping originates from spin-orbit coupling, and can be further classified into **intrinsic** (sample-growth independent) and **extrinsic** (sample-growth dependent) damping. The extrinsic damping results from magnon scattering with phonons from structural defects, surface roughness and sample inhomogeneities.

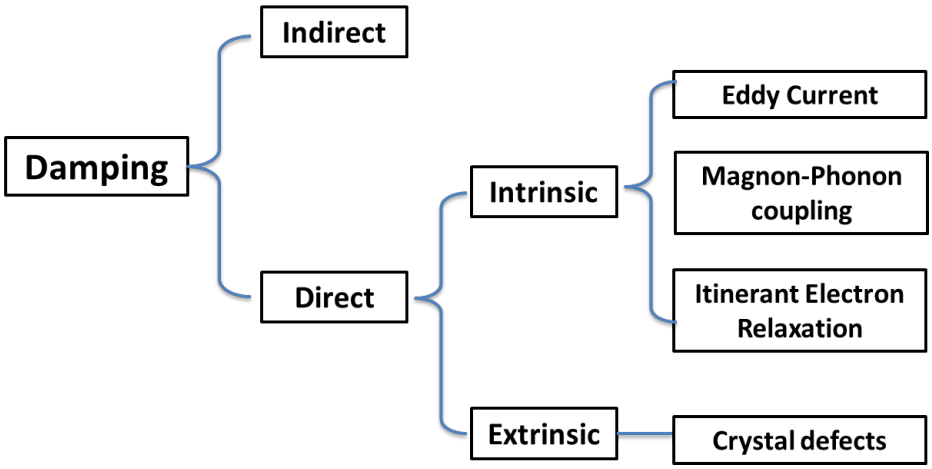

Figure 3.1: Classification of damping mechanism.

The intrinsic damping mechanism includes unavoidable processes such as electron scattering by phonons and magnons in the lattice. These processes determine the Gilbert damping parameter.

The damping parameter measured in the experiment is defined as the effective damping constant which includes both intrinsic and extrinsic damping mechanism, $\alpha_{eff} = \alpha_{in} + \alpha_{ex}$. The value of the Gilbert damping constant is estimated by the smallest measured value of α_{eff}.

3.2 Physical origin of intrinsic damping

Three major mechanisms contribute to the intrinsic damping in ferromagnetic materials. These are (i) eddy currents, (ii) magnon-phonon coupling, and (iii) itinerant electron relaxation. In the following subsections all three mechanisms will be introduced with respect to their relevance to ultrathin ferromagnetic films.

3.2.1 Eddy currents

Eddy currents (also called Foucault currents) are electric currents induced within conductors by a changing magnetic field in the conductor. In the ferromagnetic material, the local magnetic field fluctuating with the magnetization precession motion induces the Eddy current. The contribution of eddy currents to the equation of motion can be evaluated by integrating Maxwells equations across the film thickness t_F

[9]. The Gilbert damping constant resulting from the effective field can be written into this form:

$$\alpha_{eddy} = \frac{1}{6} M_s \gamma (\frac{4\pi}{c})^2 \sigma t_F^2 \tag{3.1}$$

Here, σ is the electrical conductivity and c is the velocity of light. Normally, the eddy current contribution only becomes comparable to the intrinsic damping for samples thicker than 50 nm.

3.2.2 Magnon-phonon coupling

Magnon-phonon scattering is another possible relaxation mechanism for the intrinsic damping. The calculation for the magnon relaxation by phonon drag was presented by H. Suhl in *Theory of the magnetic damping constant.*

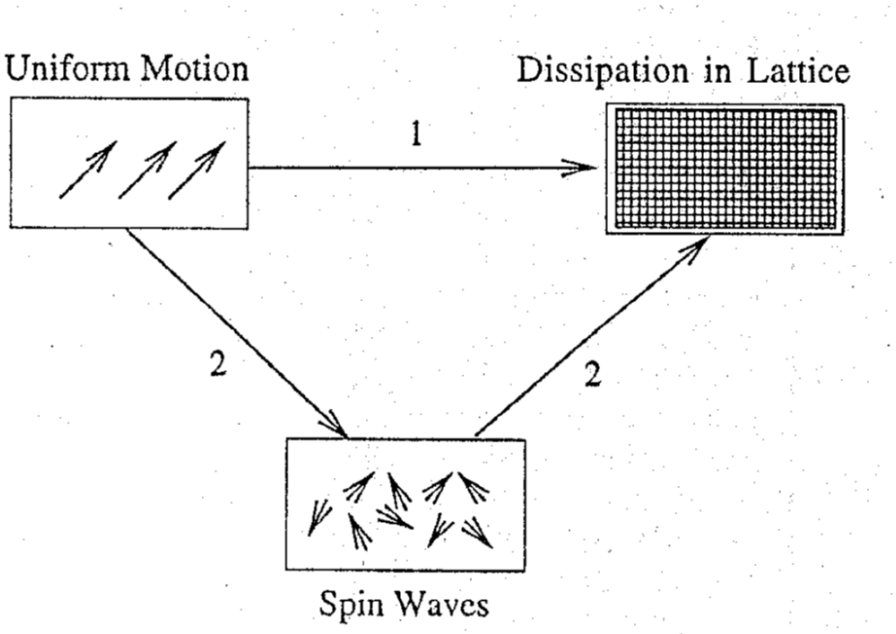

Figure 3.2: Two paths for degradation of uniform motion: (1) Direct relaxation to the lattice; (2) Decay into non-uniform motions, which in turn decays to the lattice. From [10].

As shown in the Fig. 3.2, there are two main pathways for degradation of the uniform mode. Energy flows from the uniform mode into lattice motions (phonons).

Alternatively, energy flows into the non-uniform magnetic mode (magnon). Eventually, these modes decay to the lattice. In the latter case there is a delay for the lattice motion (phonons), called phonon drag. This non-linear contribution can be written as

$$\alpha_{phonon} = \frac{2\eta\gamma}{M_s} \cdot \frac{B^2(1+\nu)^2}{E^2} \tag{3.2}$$

where η is the phonon viscosity, B is the magneto-elastic shear constant, E is the Young modulus, and ν is Poisson's ratio. All parameters are accessible except for the phonon viscosity η.

3.2.3 Itinerant electrons

The most important damping mechanism in ultrathin metallic ferromagnets is the itinerant electron interaction proposed by Heinrich et al [11]. It is assumed that there are two kinds of electrons, localized (d-electrons) and itinerant (s-electrons).

Spin-flip scattering: s-d interaction

The s-d exchange interaction can be obtained by integrating the s-d exchange energy density. The Hamiltonian is given by three particle collision terms

$$\mathcal{H} = \sqrt{\frac{2S}{N}} \sum_k J(\mathbf{q}) a_{k,\uparrow} a^+_{k+q,\downarrow} b_q + (h.c.) \tag{3.3}$$

where N is the number of atomic sites, S is the spin of d-electrons, $J(\mathbf{q})$ is the s-d exchange constant, a and a^+ are the respective annihilation and creation operations of itinerant electrons while the wave vectors $\mathbf{k}$ and $\mathbf{k}+\mathbf{q}$ have the appropriate spin $\uparrow,\downarrow$. Here the operator b annihilates the magnon with wave vector $\mathbf{q}$.

As shown in the Fig. 3.3, a magnon with energy $\hbar\omega_{\mathbf{q}}$ collides with an itinerant electron of energy $\varepsilon_{\mathbf{k}}$ and spin $\uparrow$. This results in annihilation of the magnon and creation of an electron-hole pair. The excited electron carries the energy $\varepsilon_{\mathbf{k}+\mathbf{q}}$ and spin $\downarrow$. Because the total spin angular momentum in the collision is conserved, the electron spin flip is necessary for the annihilation of a magnon.

We need to take into account the finite lifetime of electron-hole pairs due to the scattering by thermally excited phonons and magnons. This can be done by adding an imaginary term in the electron-hole pair energy,

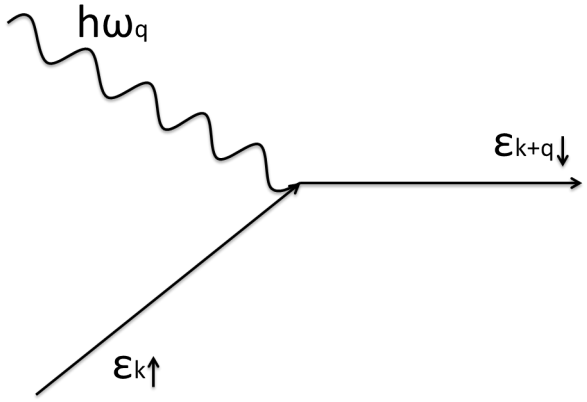

Figure 3.3: Feynman diagram of the three-particle collision.

$$\Delta\varepsilon_{\mathbf{k},\mathbf{k+q}} = \varepsilon_{\mathbf{k+q},\downarrow} - \varepsilon_{\mathbf{k},\uparrow} + i\frac{\hbar}{\tau_{sf}} \tag{3.4}$$

where τ_{sf} is the spin relaxation time.

The Green function formalism in the Random Phase Approximation (RPA) is used to calculate the Gilbert damping parameter [12]. The damping parameter α can be expressed by the effective damping field H_{eff}^{sf} due to spin-flip scattering,

$$H_{eff}^{sf} = \alpha\frac{\omega}{\gamma} = \frac{2\overline{S}}{Ng_{\mu_B}}\hbar\omega_k\sum_k |J(\mathbf{q})|^2|\frac{dn}{d\varepsilon}|L \tag{3.5}$$

where the summation is carried out over all available states at the Fermi surface. $\overline{S} = M_s(T)/M_s(0)$ is the reduced spin S, and n is the density of states(DOS). We use the factor $g\mu_B = \gamma\hbar$ to convert the energy into an effective field. The probability of energy-conserved scattering is represented by the Lorentzian factor L in (3.5)

$$L = \frac{\hbar}{\tau_{sf}}\frac{1}{(\hbar\omega_k + \varepsilon_{\mathbf{q},\uparrow} - \varepsilon_{\mathbf{k+q},\downarrow})^2 + (\frac{\hbar}{\tau_{sf}})^2} \tag{3.6}$$

Substituting (3.6) into (3.5), we can simplify this by neglecting the higher order term $(\frac{\hbar}{\tau_{sf}})^2$. Assuming a Fermi distribution of the form,

$$|\frac{dn}{d\varepsilon}| = \delta(\varepsilon_k - \varepsilon_F) \tag{3.7}$$

where δ is the Dirac delta function and ε_F is the Fermi energy. Equation (3.5)

can be rewritten as,

$$H_{eff}^{sf} = \frac{2\overline{S}}{Ng_{\mu_B}}\hbar\omega_k \sum_k |J(\mathbf{q})|^2 \delta(\varepsilon_k - \varepsilon_F)\hbar\omega_q \frac{\hbar}{\tau_{sf}} \frac{1}{(\hbar\omega_k + \varepsilon_{\mathbf{q},\uparrow} - \varepsilon_{\mathbf{k}+\mathbf{q},\downarrow})^2} \tag{3.8}$$

Here we assume that the sample magnetization response is nearly homogenous, i.e., $q \to 0$. The difference in electron energies in a spin-flip process is dominated by the exchange energy,

$$\hbar\omega_k + \varepsilon_{\mathbf{q},\uparrow} - \varepsilon_{\mathbf{k}+\mathbf{q},\downarrow} \approx \varepsilon_{\mathbf{q},\uparrow} - \varepsilon_{\mathbf{k}+\mathbf{q},\downarrow} = -2\overline{S}J(0) \tag{3.9}$$

Assuming unit volume and using $N\overline{S}g\mu_B = M_s$,

$$H_{eff}^{sf} = \frac{\hbar^2\omega}{2M_s\tau_{sf}} \sum k\delta(\varepsilon_k - \varepsilon_F) \tag{3.10}$$

We see that in (3.10) H_{eff}^{sf} is directly proportional to ω and inversely proportional to M_s. Comparing this with the general definition of damping parameter G, we obtain the value of damping constant α

$$G = \frac{\chi_p}{\tau_{sf}} \;\Rightarrow\; \alpha = \frac{G}{\gamma M_s} = \frac{\chi_P}{\gamma M_s \tau_{sf}} \tag{3.11}$$

where χ_P is the Pauli susceptibility of the itinerant electrons and can be calculated by integration over an appropriate Fermi surface.

$$\chi_P = (\frac{\hbar\gamma}{2\pi})^2 \int k^2 \delta(\varepsilon_k - \varepsilon_F)dk = \mu_B^2 n(\varepsilon_F) \tag{3.12}$$

where $n(\varepsilon_F)$ is the density of states at the itinerant electron Fermi level.

FM	g	l_{sd}[nm]	β	τ_{sf}[ps]	$G[10^7 Hz]$	$\alpha[10^{-3}]$	$M_s[emu/cm^3]$
Fe	2.09				5.8	2	1710
Co	2.18	59	0.36	3.8	30	11	1425
Ni	2.21				25	19	485
Py	2.14	4.3	0.73	0.03	9	6	860

Table 3.1: Spin relaxation times and other relevant parameters for several ferromagnetic materials. Py indicates permalloy, the alloy $Ni_{80}Fe_{20}$. From [9].

Table 3.1 lists s-d model calculation values of spin relaxation times and the damping parameters for several ferromagnetic materials.

Non spin-flip scattering: breathing Fermi surface

The Fermi surface of a ferromagnet in an external magnetic field is influenced by the dipole, Zeeman and spin-orbit interaction energies. In the previous s-d interaction model, the Fermi surface is assumed to be independent of the external field. In reality, changes in the magnetization orientation during the precession of magnetization or propagation of spin waves cause deformation of the Fermi surface, as shown in the Fig. 3.4. As the magnetization precession evolves in time and space, the Fermi surface also changes periodically in time and space, referred to as the *breathing Fermi surface*.

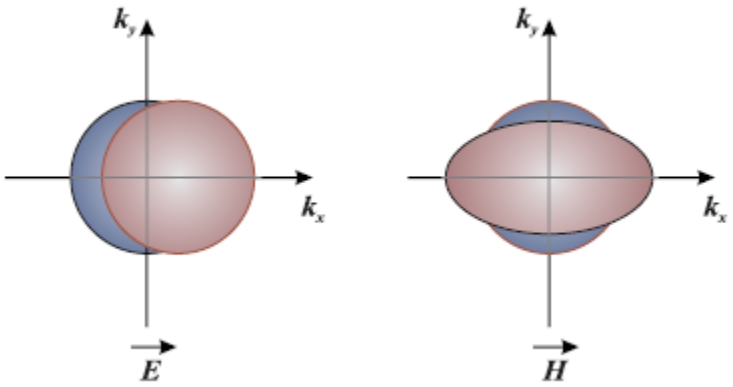

Figure 3.4: Deformations of Fermi surface in an external electric and magnetic field. From [13].

Kambersky introduced this new approach to the theory of magnetic damping in the 1970s [14]. It includes energy estimation based on Clogston's valence-exchange semiclassical method in ferrites. This original breathing Fermi surface model was improved by the *ab initio* density-functional theory using single-electron functions to describe electron scattering, introduced by Fahnle and coworkers [15]. Results of their work are presented below.

The effective magnetic field H_{eff} can be described by the magnetization orientation $\hat{n} = \mathbf{M}/M_s$,

$$H_{eff} = -\frac{1}{M_s \Omega} \sum_{k,u} n_{k,u} \frac{\partial \varepsilon_{k,u}}{\partial \hat{n}} \tag{3.13}$$

Here $(\mathbf{k}, u)$ refers to the electrons in a band with the index u and a wavevector

k. $n_{k,u}$ is the population number, $\varepsilon_{k,u}$ is the energy of the electron state and Ω is the volume of the sample.

This population number $n_{k,u}$ relaxes towards the instantaneous equilibrium value by means of an electron-phonon scattering process. The phase lag between the actual electron population and the population corresponding to the instantaneous magnetization direction leads to the magnetic damping.

The variation of the total electron energy density ε is

$$\varepsilon = \Omega^{-1} \sum_{k,u} \varepsilon_{k,u} n_{k,u} \tag{3.14}$$

And the non-equilibrium populations $n_{k,u}$ are approximately given by Boltzman's equation,

$$n_{k,u} = f_{k,u} - \tau_{k,u} \frac{\partial f_{k,u}}{\partial t} \tag{3.15}$$

where $f_{k,u} = f(\varepsilon_{k,u})$, $f(\varepsilon)$ is the Fermi function and $\tau_{k,u}$ is the lifetime of the appropriate electron state. Substituting (3.15) into (3.13) and using the chain rule, we obtain

$$H_{eff} = -\frac{1}{M_s \Omega} \sum_{k,u} \tau_{k,u} - (\frac{\partial f(\varepsilon_{k,u})}{\partial \varepsilon_{k,u}}) \frac{\partial \varepsilon_{k,u}}{\partial \hat{n}_i} \frac{\partial \varepsilon_{k,u}}{\partial \hat{n}_j} \frac{\partial \hat{n}_j}{dt} \tag{3.16}$$

Simplifying the equation (3.16) with the delta equation $-\partial f(\varepsilon_{k,u})/\partial \varepsilon_{k,u} \approx \delta(\varepsilon_F - \varepsilon_{k,u})$ and using the same effective lifetime τ for all the states, we obtain the expression of damping parameter α

$$\alpha = \frac{\tau \gamma}{M_s \Omega} \sum_{k,u} \delta(\varepsilon_F - \varepsilon_{k,u}) (\frac{\partial \varepsilon_{k,u}}{\partial \hat{n}_j})^2 \tag{3.17}$$

The scattering process in this model includes only electrons near the Fermi surface, which allows only intraband scattering contribution to the damping. Therefore, this model only considers the nearly adiabatic process.

3.3 Extrinsic damping

Extrinsic damping in the ferromagnetic film can be influenced by deposition parameters or doping with impurities, which offers one way to tune the damping constant

in memory devices.

3.3.1 Doping

Doping materials can result in a lattice constant mismatch, changing the defects distribution in the lattice.

For example, $(Ni_{80}Fe_{20})_{100-x}Pt_x$ films have been deposited to investigate the effects of Pt doping in the permalloy [16]. The experimental result shows that value of the damping constant α rises to 0.06 from 0.01 with increasing Pt concentration from $x = 0$ to $x = 34$.

3.3.2 Annealing temperature

Different sample deposition and annealing conditions will lead to various film surface roughness. Recent studies suggest that the effective damping constant in a Co_2MnAl Heusler alloy film depends on the annealing temperature. [17] The 50 nm-thick films were grown on SiO_2 substrates by magnetron sputtering.

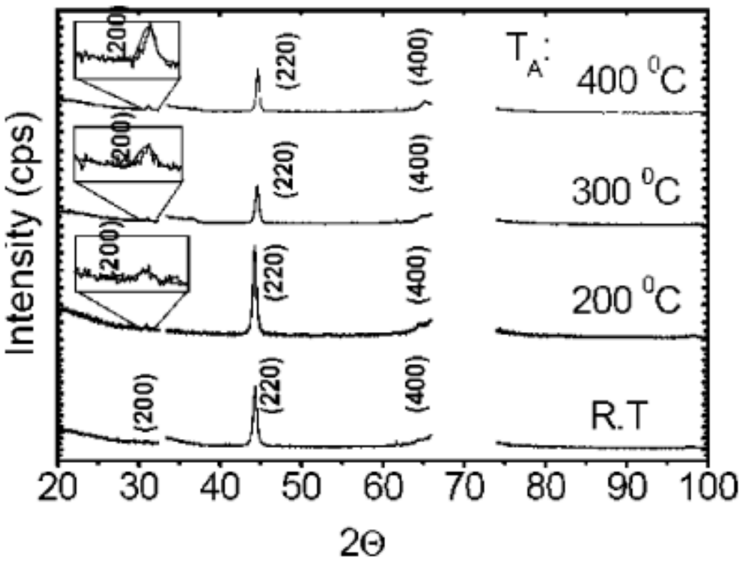

Figure 3.5: XRD pattern of Co_2MnAl films at room temperature and several annealing temperatures. From [17]

The X-ray Diffraction (XRD) spectra in Fig.3.5 shows that the film grown on a room temperature substrate had an A2(220) structure, whereas the degree of B2(200)

order increased with increasing annealing temperature.

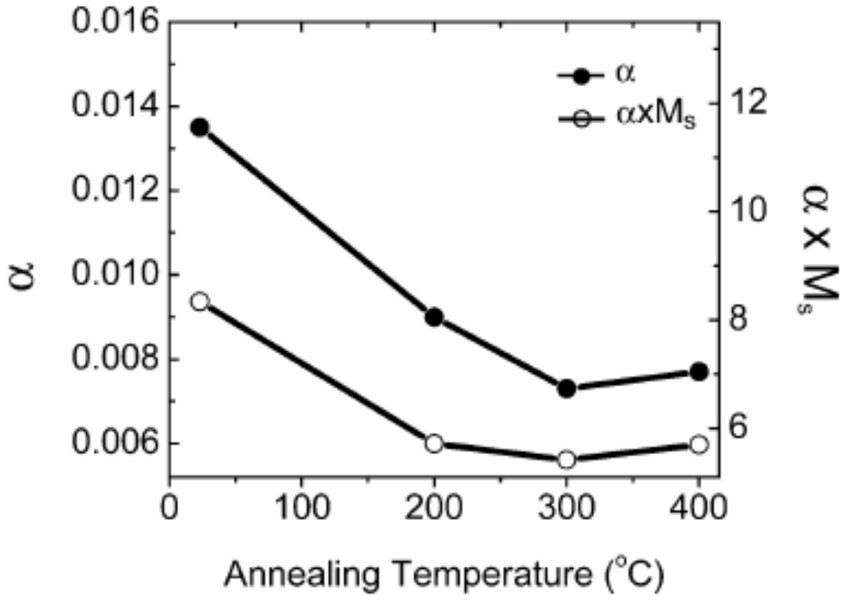

Figure 3.6: Annealing temperature dependence of damping constant α and αM_s. From [17]

The damping constant in Fig.3.6 is measured by ferromagnetic resonance technique (FMR). It was found that the damping constant decreased with increasing annealing temperature and showed a minimum value of 0.007 for a 300 °C annealing temperature. The B2 chemical order induced by annealing process affects the damping property sensitively, which can be explained by the extrinsic damping dependence on lattice defects.

Chapter 4

Experimental methodology

4.1 Sample preparation

This section summarizes the sample preparation process.

4.1.1 Physical vapor deposition

Physical vapor deposition (PVD) generally refers to depositing a film of specific material on wafers in a high vacuum environment. The coating method can be high temperature evaporation, or plasma sputter bombardment.

Electron beam evaporation

In the electron beam physical vapor deposition (EBPVD) system, we use a charged tungsten filament to generate a high-intensity electron beam in high vacuum. The target material contained in a water-cooled crucible is heated by the focused electron beam and vaporized into the gaseous phase. This material vapor condenses to form a uniform thin film on the substrate. Within this process, the deposition rate is monitored by a quartz crystal microbalance (QCM) sensor, whose resonant frequency is sensitive to the deposition thickness [18].

Samples using this technique are made in house.

Parameter	Value
Initial base pressure	$1.0 - 2.0 \times 10^{-7}$ Torr
Deposition base pressure	$1.0 - 2.0 \times 10^{-6}$ Torr
Deposition rate	1 Å/s
Electron acceleration voltage	25 kV

Table 4.1: Electron beam evaporation parameters.

Magnetron sputtering

In a sputter deposition system, ionized inert gas atoms (e.g. Argon) confined by the magnetic field bombard the target slab. Subsequently, free atoms released from the target slab will condense onto the sample substrate. Compared to thermal evaporation, magnetron sputtering gives rise to the smoother film surface.

Samples using the sputtering technique are made at the University of Alabama.

4.1.2 Nanofabrication

Here, I summarize the basic procedure of spin coating, fabrication and lift-off technique, which is generally used in the nanostructure fabrication. All the samples were patterned at the UVic nanofab.

4.1.3 Electron beam lithography

Fig.4.1 illustrates the general fabrication procedure. More details are listed below:

(a) Spin coat the wafer with two uniform layers of poly-methyl-methacrylate (PMMA) as the electron beam resist. (The bottom layer with lighter molecular weights is more sensitive to the electron beam.)

(b) Design a pattern in the software and expose PMMA of the pattern area to electron beam. (The high-energy electron beam will break chemical bonding in the PMMA, which can be subsequently removed with an appropriate developer solution.)

(c) Deposit the target material on the patterned substrate in the electron beam evaporation or sputtering system with the deposition thickness around one-third of the resist dwell depth.

(d) Wash the residual PMMA away with acetone to accomplish the lift-off

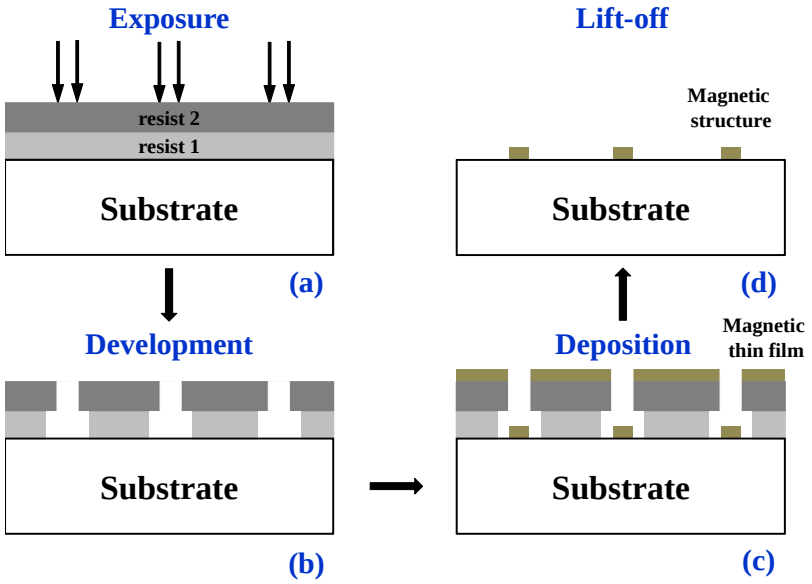

Figure 4.1: General fabrication process.

4.2 Characterization of magnetic properties: Magneto-Optic Kerr Effect

4.2.1 History of magneto-optics

- 1845 **Magneto-optic Faraday effect**: Whereby the plane of polarization of the transmitted light is rotated when the light travels through a magnetic medium.
- 1876 **Kerr effect**: Similar to the Faraday effect, whereby light reflected from a magnetized material has a rotated plane of polarization and ellipticity.
- 1899 **Voigt effect**: Similar to the Faraday effect, except Voigt effect is quadratic in **M** while the Faraday effect is linear in the applied magnetic field.

4.2.2 Classification

The magneto-optic Kerr Effect (MOKE) can be further categorized by the direction of the magnetization vector with respect to the reflecting surface and the plane of incidence. Three kinds of geometries are possible, named polar, longitudinal and transverse, as shown in Fig 4.2.

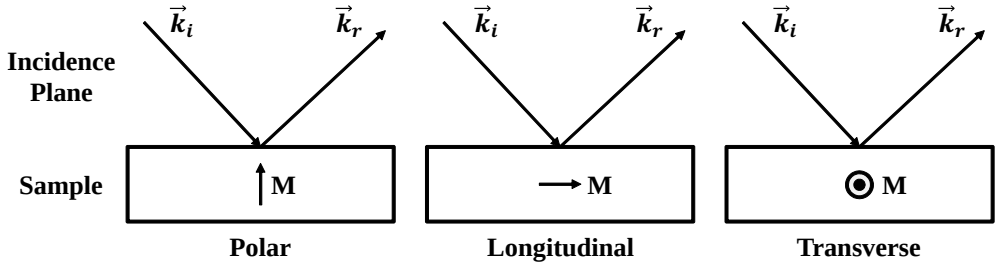

Figure 4.2: Three MOKE geometries.

Here, $\mathbf{k}_i$, $\mathbf{k}_r$ are the incident and reflection light vectors respectively.

4.2.3 Fresnel equation

The Kerr and Faraday effects appear because left- and right-circularly polarized light waves propagate differently in a magnetic material. The propagation of the electromagnetic wave is governed by the Maxwell equations,

$$\begin{aligned} \nabla \times \mathbf{H} &= \frac{4\pi}{c}\mathbf{j} + \frac{1}{c}\frac{\partial \mathbf{D}}{\partial t} \\ \nabla \times \mathbf{E} &= -\frac{1}{c}\frac{\partial \mathbf{B}}{\partial t} \end{aligned} \tag{4.1}$$

with $\mathbf{D}$ the electric displacement, $\mathbf{E}$ the electric field, $\mathbf{B}$ the magnetic induction, $\mathbf{H}$ the magnetic field and $\mathbf{j}$ the current density.

Apart from Maxwell equations, there are material equations which relate $\mathbf{D}$, $\mathbf{j}$, $\mathbf{B}$ with $\mathbf{E}$ and $\mathbf{H}$.

$$\mathbf{D} = \epsilon\mathbf{E},\ \mathbf{j} = \sigma\mathbf{E},\ \mathbf{B} = \mu\mathbf{H} \tag{4.2}$$

Here, ϵ is the dielectric tensor, μ is the magnetic permeability tensor and σ is the conductivity tensor.

Substituting (4.2) into (4.1), we obtain,

$$-\nabla^2\mathbf{E} + \nabla(\nabla \cdot \mathbf{E}) = -\frac{1}{c^2}\frac{\partial^2 \mathbf{D}}{\partial t^2}. \tag{4.3}$$

The propagation of normal light modes in a medium is described by the Fresnel

equation. We define the vector refractive index as $\mathbf{n} = c\mathbf{k}/\omega$, which depends on both $\mathbf{k}$ wave vector and the frequency ω.

The electric wave field in the medium is thus,

$$\mathbf{E}(\mathbf{r}, t) = E_0 e^{i\omega \mathbf{n}\cdot\mathbf{r}/c - i\omega t} \tag{4.4}$$

where $\mathbf{n}(\omega)$ is to be determined. Substituting (4.4) into (4.3), we obtain the Fresnel equation,

$$[n^2 \cdot \mathbb{1} - \boldsymbol{\epsilon} - \mathbf{n} : \mathbf{n}] \cdot \mathbf{E} = 0 \tag{4.5}$$

here $\mathbf{n} : \mathbf{n}$ is the dyadic product, i.e.,$n_i n_j$.

The simplest solution to the Fresnel equation is a non-magnetic and isotropic medium (i.e., $\epsilon = \epsilon_0 \cdot \mathbb{1}$) and the only solution is $n_0^2 = \epsilon_0$, where n_0 is the refractive index of the nonmagnetic medium.

The solution varies with the different symmetry of the dielectric tensor ϵ, which depends on external fields, $\epsilon \to \epsilon(\mathbf{k}, \omega, \mathbf{B}, \mathbf{E})$.

$$\begin{aligned} \epsilon(\mathbf{k}, \omega, \mathbf{B}, \mathbf{E}) \approx\ & \epsilon_0 \quad \text{[constant]} \\ & + \mathcal{O}(\mathbf{k}) + \mathcal{O}(\mathbf{B}) + \mathcal{O}(\mathbf{E}) \quad \text{[linear]} \\ & + \mathcal{O}(B_i E_j) + \mathcal{O}(B_i B_j) + \mathcal{O}(k_i B_j) + ... \quad \text{[quadratic]} \end{aligned} \tag{4.6}$$

Here, $\mathcal{O}(\mathbf{k}), \mathcal{O}(\mathbf{B}), \mathcal{O}(\mathbf{E})$ refer to the Snell's refraction, magneto-optical Faraday(Kerr) effects and electro-optical effects, respectively. Quadratic terms give rise to the Voigt effect and other non-linear effects.

4.2.4 Kerr rotation and Kerr ellipticity

Polar MOKE

Generally, non-magnetic crystal symmetries give diagonal dielectric tensors. However, magnetization will induce off-diagonal terms. For example, a ferromagnetic material magnetized along the z-axis has a dielectric tensor of this form,

$$\epsilon = \begin{pmatrix} \epsilon_{xx} & \epsilon_{xy} & 0 \\ -\epsilon_{xy} & \epsilon_{xx} & 0 \\ 0 & 0 & \epsilon_{zz} \end{pmatrix} \tag{4.7}$$

where the off-diagonal element ϵ_{xy} is linearly dependent on the magnetization $\mathbf{M}$ in the ferromagnetic material.

In the polar-MOKE case where the incident light is perpendicular to the medium interface, the refractive index $\mathbf{n} = c\mathbf{k}/\omega = n\mathbf{e}_z$. Substituting these into (4.5), we obtain the solution for the complex refractive index $\mathbf{n}$ and normalized eigenmodes of electromagnetic wave in the magnetic materials [19].

$$n_{\pm}^2 = \epsilon_{xx} \pm i\epsilon_{xy}, \quad \begin{pmatrix} E_x \\ E_y \end{pmatrix} = \frac{1}{\sqrt{2}} \begin{pmatrix} 1 \\ \pm i \end{pmatrix}, \; E_z = 0 \tag{4.8}$$

The second equation in (4.8) represents left- and right-handed circularly polarized light. The left-hand with helicity + corresponds to n_+, the other one with helicity $-$ to n_-. The different absorption of left and right circularly polarized light is called *circular dichroism*.

The Kerr rotation θ_K and ellipticity ϑ_K for most magnetic materials are less than 1^o. With the approximation for small θ_K, ϑ_K, we obtain,

$$\theta_K + i\vartheta_K \simeq i\frac{(n_+ - n_-)n_0}{(n_+n_- - n_0^2)} \tag{4.9}$$

which proves that the difference in the propagation of the two normal modes in the material leads to the MO Kerr effect. Often the Voigt parameter $Q \equiv i\epsilon_{xy}/\epsilon_{xx} \simeq (n_+ - n_-)/\overline{n}$ with $\overline{n} \equiv \sqrt{\epsilon_{xx}}$ is introduced to rewrite the equation (4.9), which leads to

$$\theta_K + i\vartheta_K \simeq \frac{-in_0\overline{n}Q}{\overline{n}^2 - n_0^2} = \frac{-\epsilon_{xy}(\mathbf{M})\epsilon_0}{\sqrt{\epsilon_{xx}}(\epsilon_0 - \epsilon_{xx})} \tag{4.10}$$

Obviously, the Kerr rotation has a linear response to the magnetization rotation in the ferromagnetic material. Because only the off-diagonal term ϵ_{xx} depends on the magnetization rotation.

Longitudinal MOKE

For the longitudinal MOKE, we set the incidence in the y-z coordinate plane and the magnetization along the y-axis. The dielectric tensor adopts the form

$$\epsilon = \begin{pmatrix} \epsilon_{xx} & 0 & \epsilon_{xz} \\ 0 & \epsilon_{yy} & 0 \\ -\epsilon_{xz} & 0 & \epsilon_{zz} \end{pmatrix} \tag{4.11}$$

Following the same recipe with polar MOKE, we can write down the solution for longitudinal MOKE,

$$n_{\pm}^2 = \epsilon_{xx} \pm i\epsilon_{xy} \sin\phi_r \tag{4.12}$$

with ϕ_r the incident angle.

4.2.5 Detection of the Kerr rotation

For static hysteresis measurements, the longitudinal MOKE setup was used with the external magnetic field parallel to the sample film.

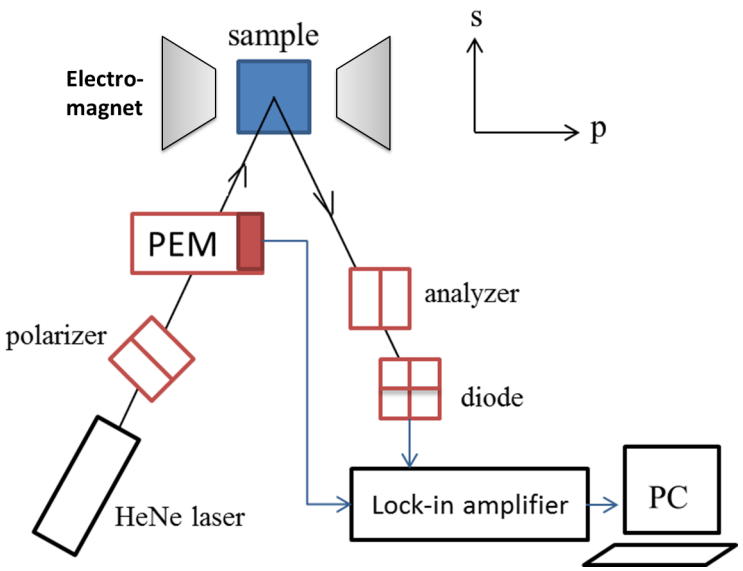

Figure 4.3: Static MOKE setup.

As shown in Fig. 4.3 and Fig. 4.4, the Kerr rotation detection is accomplished by following steps.

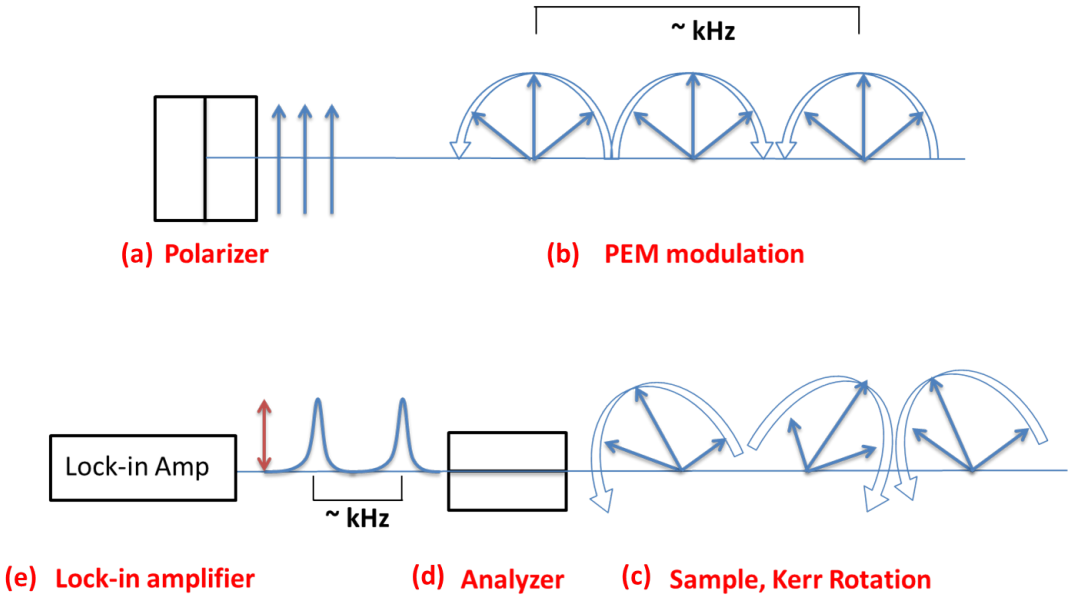

Figure 4.4: Polarization evolution schematic.

- (a) The laser beam is linearly polarized by the initial polarizer.
- (b) The PEM (Photoelastic Modulator) modulates the linearly polarized beam into equal-intensity left- and right-hand circularly-polarized waves with kHz modulation frequency.
- (c) Two circular-polarized components interact with the magnetization in the sample dichroically, which results in the Kerr rotation.
- (d) The analyzer axis is set perpendicular to the polarizer axis to eliminate the background light. The circularly-polarized light passes through the analyzer and becomes the intensity pulse with PEM frequency on the photodiode. The intensity pulse rms amplitude is linearly proportional to the Kerr rotation orientation, which also respects the magnetization rotation in a linear relation.
- (e) The lock-in amplifier detects the pulse rms amplitude with the PEM frequency and outputs a DC voltage to the PC via a DAC box.

4.3 The stroboscopic pump-probe technique

The magneto-optic detection technique can be extended to the time-resolved regime, directly measuring the dynamic evolution of magnetic systems in response to non-equilibrium perturbations.

4.3.1 Stroboscopic technique

Topler performed the first pump-probe experiment in 1867. He used a 2s spark to initiate a sound wave and then photographed the propagation using a second spark triggered with an electrical delay.

A schematic of the pump-probe technique is presented in Fig. 4.5. We consider a magnetic system that is characterized by the dynamic response M(t) as given in Fig. 4.5(b) induced by the pump excitation shown in Fig. 4.5(a).

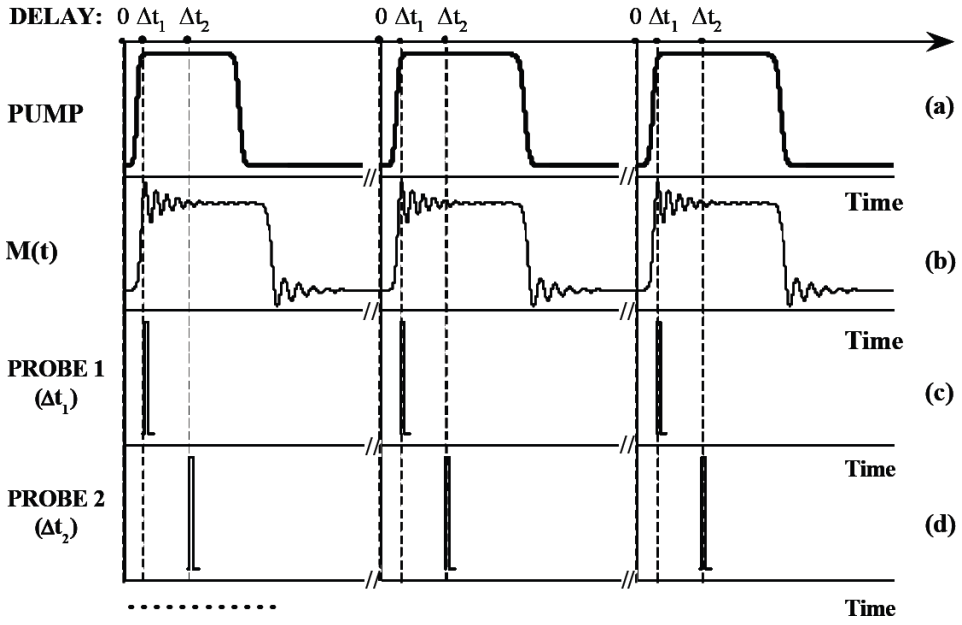

Figure 4.5: Stroboscopic pump-probe technique, from Elena [20].

M(t) is detected by a femtosecond-duration probe pulse with 20 ps temporal resolution, as shown in the Fig. 4.5(c). By changing the delay time between probe pulse and pump pulse, as shown in Fig 4.5, we can capture snapshots of $M(t_i)$ in a time series during the dynamic process, which can then be reorganized stroboscopically into the original magnetic signal.

4.3.2 Two types of pump

The main function of the pump beam is to excite the magnetic system from its initial state. Two kinds of pump excitation are used in my experiment, distinguished by their underlying physical principles: thermal demagnetization and alternating magnetic field.

All optical pump-probe

A focused infrared pulsed-laser spot can heat a magnetic sample locally above its Curie temperature. When this occurs, the ferromagnetic material will lose its magnetic order within a few picoseconds (demagnetization), and then recover, accompanied by GHz-frequency magnetization precession.

Here, we use the retroreflector to control the optical path of the pump beam. The retroreflector is moved back and forth by a stepper motor on the 2-meter track with a resistive transducer. By reading the resistance on the multimeter, we precisely control the position of the retroreflector. In this way, we finely control the time difference Δt between the pump and probe pulse. In our experimental setup, the resolution of the delay line control is around 10 ps.

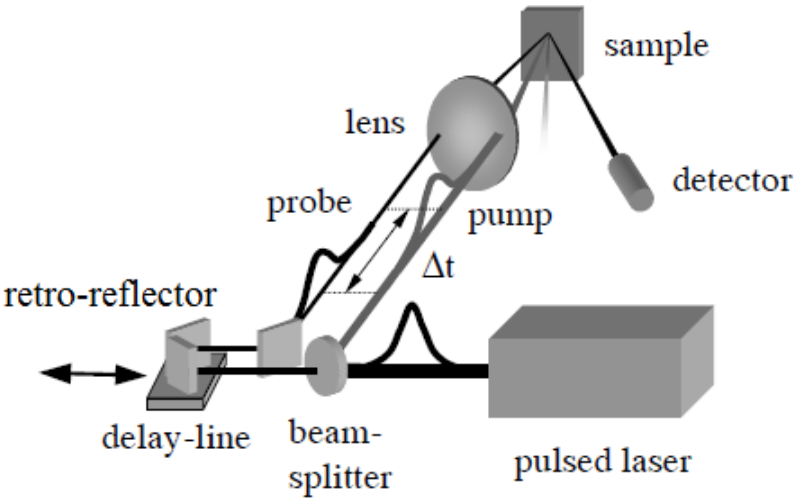

Figure 4.6: All optical pump-probe scheme, from [21].

Electric pumping

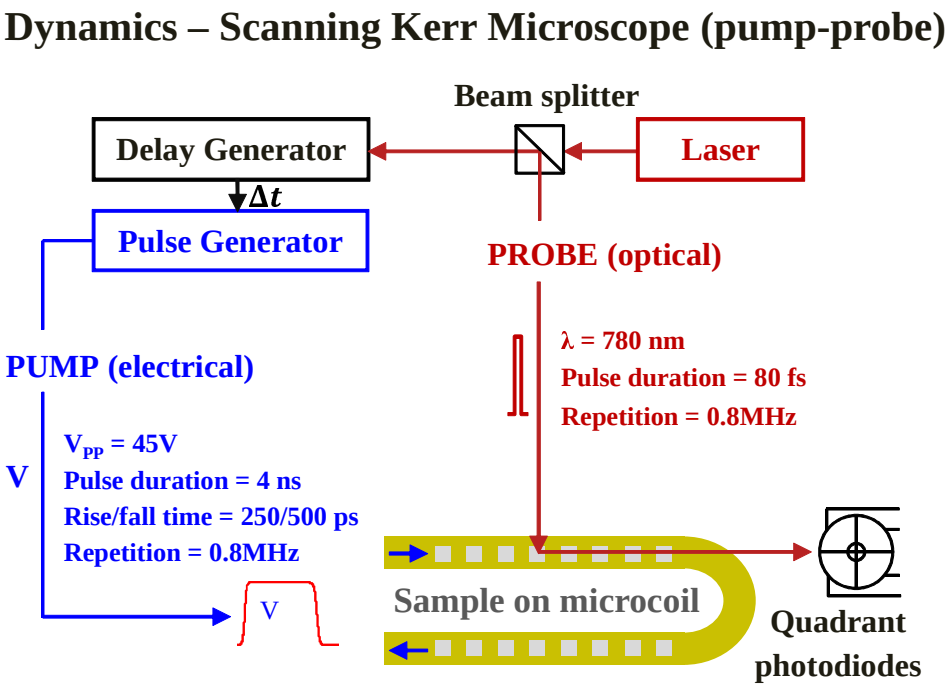

Figure 4.7: Dynamic MOKE Setup.

The electric pump-probe setup scheme is illustrated in 4.7. We introduce a beam splitter to divide the probe beam to two branches (See Fig.4.7). One is used for the magneto-optic Kerr detection, the other is used as the time reference for the pump pulse delay control. The digital delay generator is triggered by the probe time-reference signal; it adds a certain amount of time delay and feeds back to the pulse generator, which is automatically controlled by LabVIEW program.

We use a pair of quadrant photodiodes as the detector. The 5 mm-diameter spot on the four quadrants is finely balanced. With lock-in amplifiers, we can detect the magnetization component M_x, M_y, M_z, with respect to the difference with horizontal, vertical and sum outputs of the two quadrant diodes. The pump-probe setup can therefore resolve the three dimensional magnetization dynamics.

To form short magnetic field pulses at the sample, we fabricate a gold microcoil (Fig. 4.8(a)) and mount the sample on the stage connected with a printed circuit board in Fig. 4.8(b).

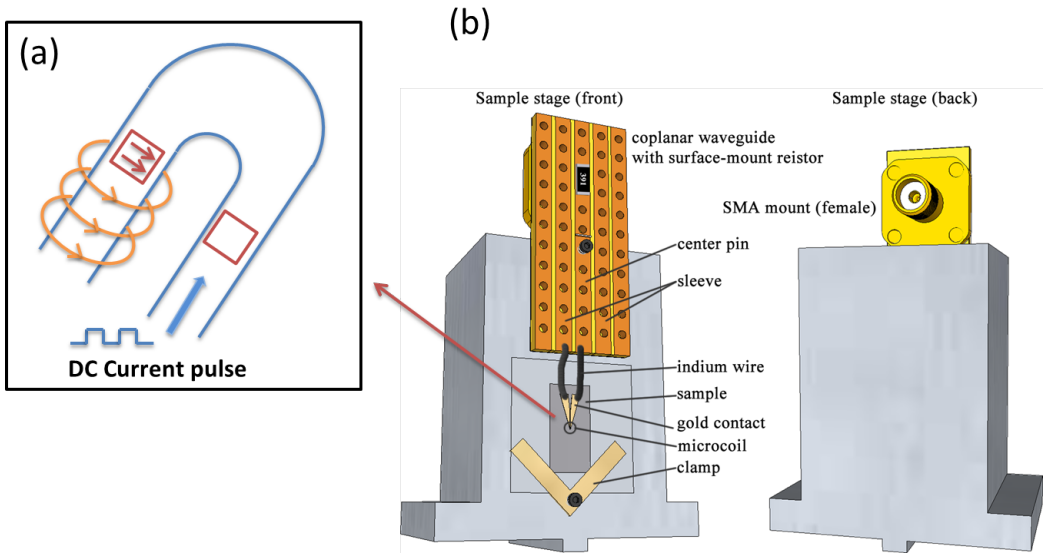

Figure 4.8: Electric pumping schematic.

By inputting the current pulse from the pulse generator to the microcoil circuit, we obtain a magnetic field pulse which quickly saturates the magnetization in the sample above the coil along the magnetic field direction. This magnetic field excitation is followed by the magnetization damped precession around the direction of the effective field.

Chapter 5

Results

Let me not pray to be sheltered from dangers,
but to be fearless in facing them.
Let me not beg for the stilling of my pain,
but for the heart to conquer it.

-Rabindranath Tagore

5.1 Reference sample: yttrium iron garnet

Pump-probe TR-MOKE is a powerful tool to detect the magnetic dynamics. Here, yttrium iron garnet(YIG) was chosen as my reference sample to prove the reliability of the experiment setup. The measurement result and analysis are shown below.

5.1.1 Fast fourier transformation: precession frequency

Using *Fast Fourier Transformation* (FFT) Matlab code to transfer the data into frequency space, the resulting major peak shows the the magnetization precession frequency. Analysing the precession frequency and external bias field, we find a square-root dependence between these two variables that is predicted by the Kittel equation.

As shown in Fig.5.2, the precession frequency increases with the bias field strength, which is consistent with the Kittel equation,

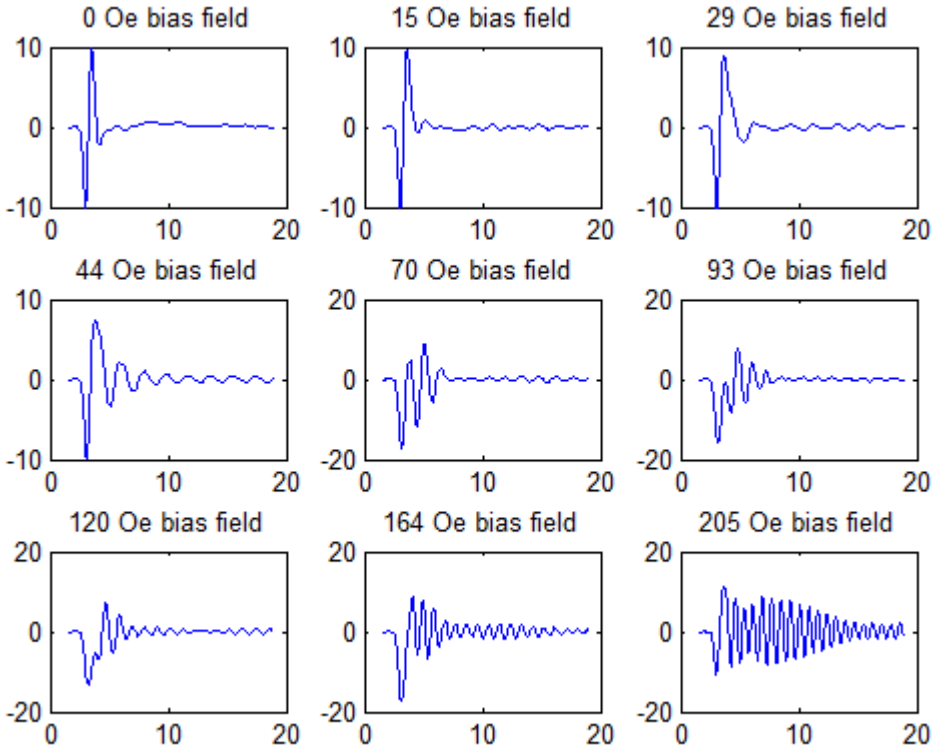

Figure 5.1: Garnet magnetization precession with different external bias fields.

$$f = \frac{\gamma}{2\pi}\sqrt{H(H + \mu_0 M_s)}. \tag{5.1}$$

Here γ is the gyromagnetic ratio, H is the effective field strength and M_s is the saturation magnetization.

5.1.2 Effective damping constant

To get the quantitative information of the Gilbert damping constant, we fit the Kerr signal to a damped-harmonic function expressed as

$$M(t) = \mathcal{A}e^{\frac{-t}{\tau}}\sin(2\pi f t + \varphi) \tag{5.2}$$

where $\mathcal{A}$ is the amplitude, τ is the relaxation time, f is the precession resonance frequency and φ is the initial phase. [22]

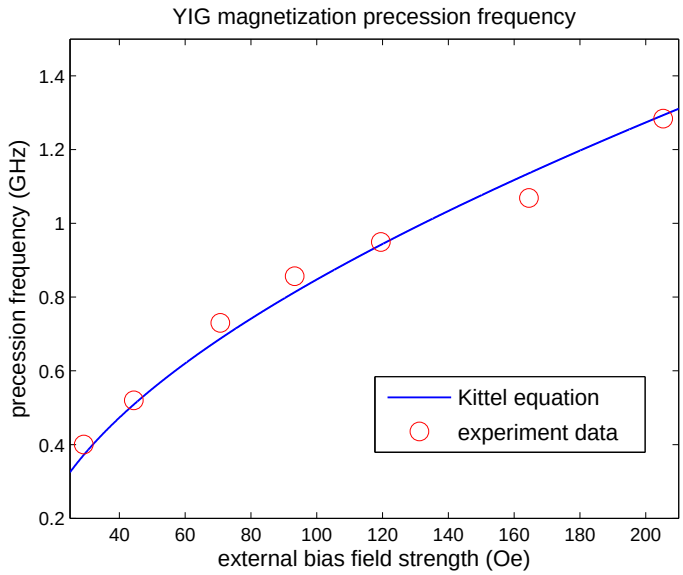

Figure 5.2: Garnet magnetization precession frequencies with different external bias fields.

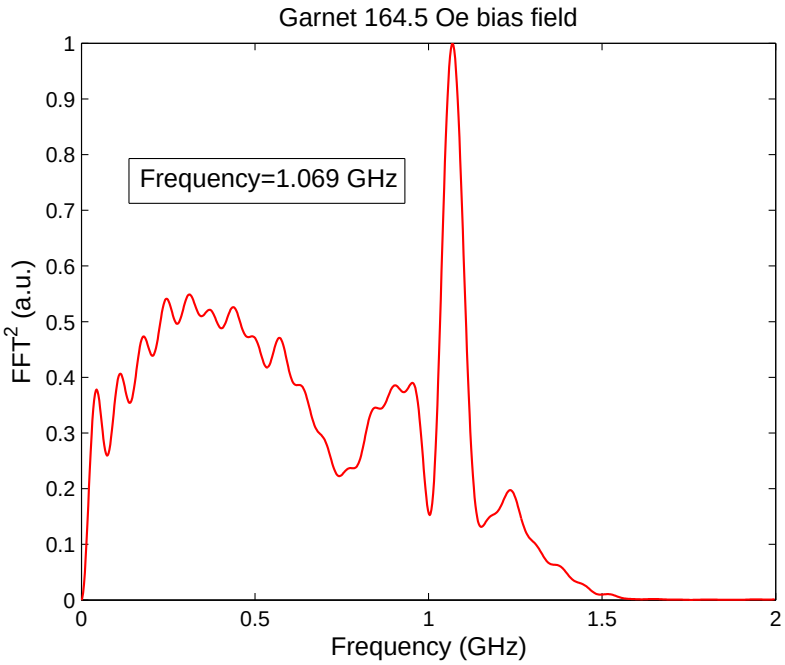

Figure 5.3: Fast Fourier transformation example.

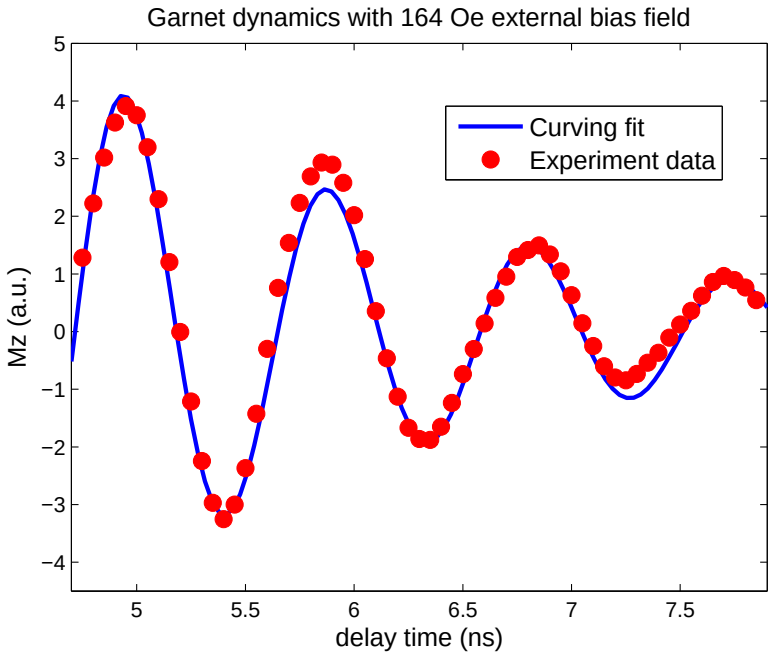

Figure 5.4: Curve fitting for YIG magnetization dynamics with 164 Oe external bias field.

As shown, f value can be obtained by Fourier transformation from the experimental data or by curving fitting parameters.

To gain quantitative information of Gilbert damping, an effective damping constant, α_{eff}, is defined as

$$\alpha_{eff} = \frac{1}{2\pi f \tau} \tag{5.3}$$

The effective damping constant α_{eff} accounts not only for the intrinsic (Gilbert) damping α but also for the extrinsic magnetic relaxation, $\alpha_{eff} = \alpha_{in} + \alpha_{ex}$. The effective damping constant varies with the external bias field strength, orientation and sample properties while the Gilbert damping constant is an intrinsic constant for certain material. The value of the Gilbert damping constant is estimated to be less than the minimum experiment value of effective damping constants.

Fig. 5.3 is the Fast fourier transformation result for the dynamics with 164 Oe bias field. The main peak shows that the magnetization precession frequency is 1.069 GHz. Yet there are several minor peaks in the plot due to the optical scattering and electronic noise.

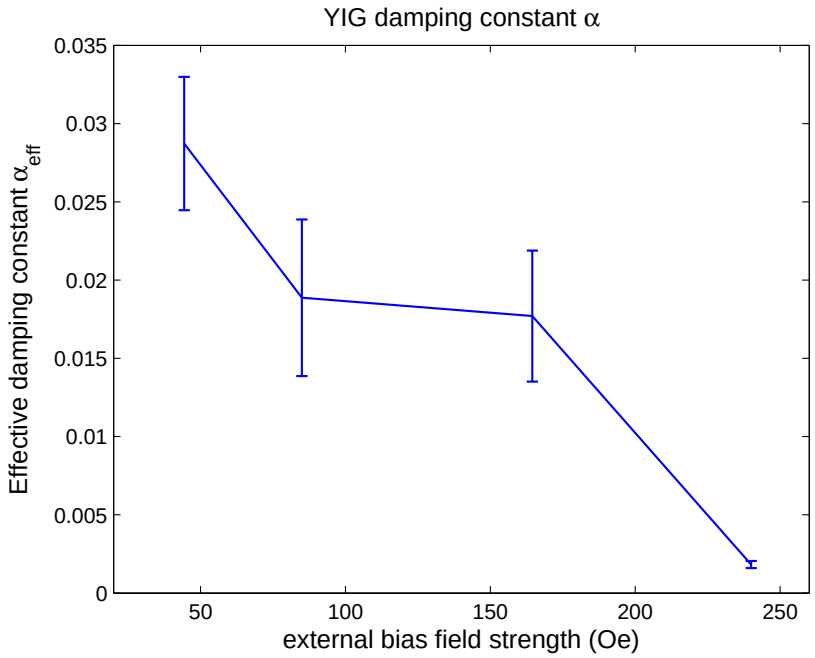

Figure 5.5: YIG effective damping constant α_{eff} with different external bias field strength. Solid line is the eye guide of the damping parameter value; error bar comes from the curve fit uncertainty.

The damped-oscillation curve fitting to the YIG magnetization dynamics with 164 Oe bias field is illustrated in Fig. 5.4. The precession frequency is 1.083 ± 0.007 GHz, the relaxation time is 1.988 ns and the effective constant is 0.0173.

From Fig. 5.5, it is found that the minimum value of effective damping constants is 0.0018 with a 205 Oe bias field. The effective damping constant in YIG film shows a monotonic decrease with the increasing bias field strength. We can compare this value of the Gilbert damping constant, 0.0005, in YIG film in [23].

The reason why my experiment value is larger than the reference value is that YIG magnetization saturates with the bias field strength around 1845 Oe and the maximum bias field in my experiment is too weak to saturate the magnetization in YIG film along bias field orientation.

5.2 Permalloy square

Using the experimental setup that has been proved by the garnet sample, we can detect the magnetization dynamics in the permalloy sample. Here the sample we use

is the 20 nm-thick $10\mu m \times 10\mu m$ Py square on top of the gold coil.

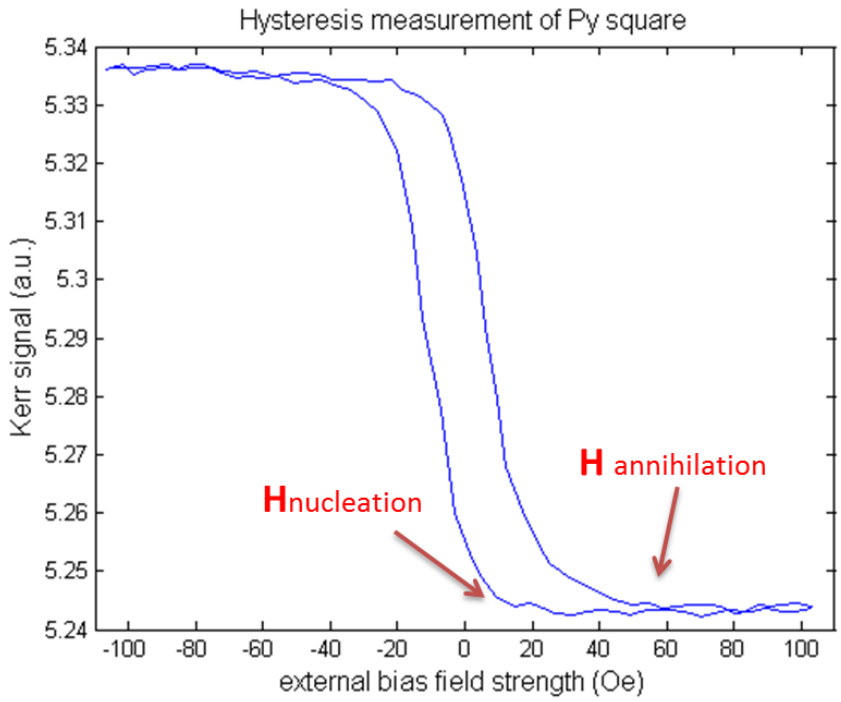

Figure 5.6: Hysteresis loop of Py square sample.

The hysteresis loop of these Py square sample is measured through a 10X microscope objective. The magnetic Kerr signal is the average result with the spot size around 50 μm. From 5.6, we find that the saturation field strength for permalloy square is around 50 Oe.

In Fig. 5.6, the hysteresis shows the annihilation character of the vortex configuration. Instead of the square shape in the Py film hysteresis, the vortex hysteresis has a curvy tail.

5.2.1 Domain configuration

In the micromagnetic simulation software, the ground state of the Py square sample is obtained by minimizing the total energy. As shown in the schematic diagram Fig. 5.7, there are four domains and a vortex core. The top and bottom domain have antiparallel orientations.

The vortex position and domain sizes are changed by applying an external bias field.

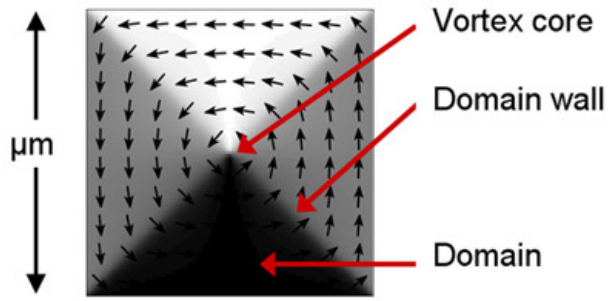

Figure 5.7: Laudau domain structure in square shape sample.

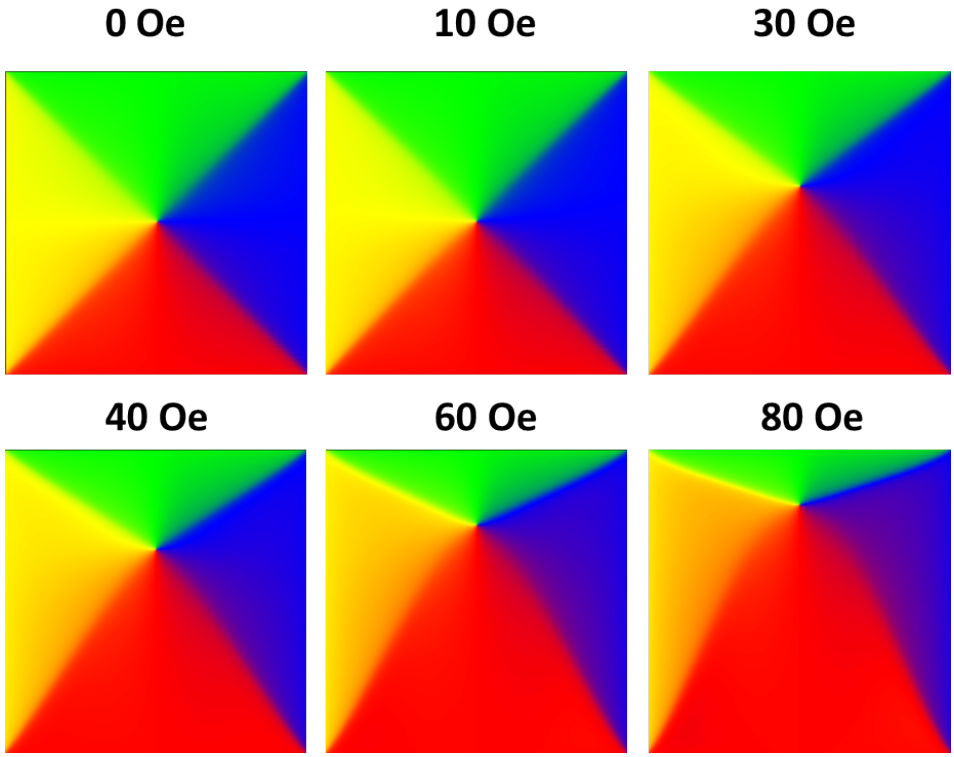

Figure 5.8: Domain configuration in the Py square.

As shown in the Fig. 5.8, by increasing the strength of the bias field antiparallel to the magnetization orientation in the bottom domain, the vortex core shifts up and the bottom domain expands.

In the experiment, according to Rayleigh Criterion, the probe laser spot size after 80X objective lens is around $1\mu m$ diameter size. By changing the focus spot position,

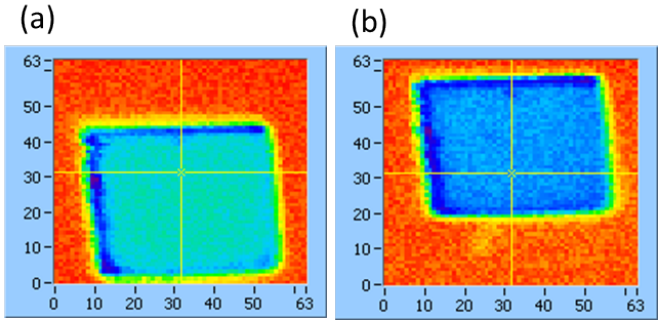

Figure 5.9: Spacial scan of the Py square without the magnetic bias field. (a) Top domain (b) Bottom domain

we can observe the magnetization dynamics in the top and bottom domain individually, as shown in the Fig. 5.9. Here the cross in Fig. 5.9 reflects the center of the probe spot.

5.2.2 Precession frequency

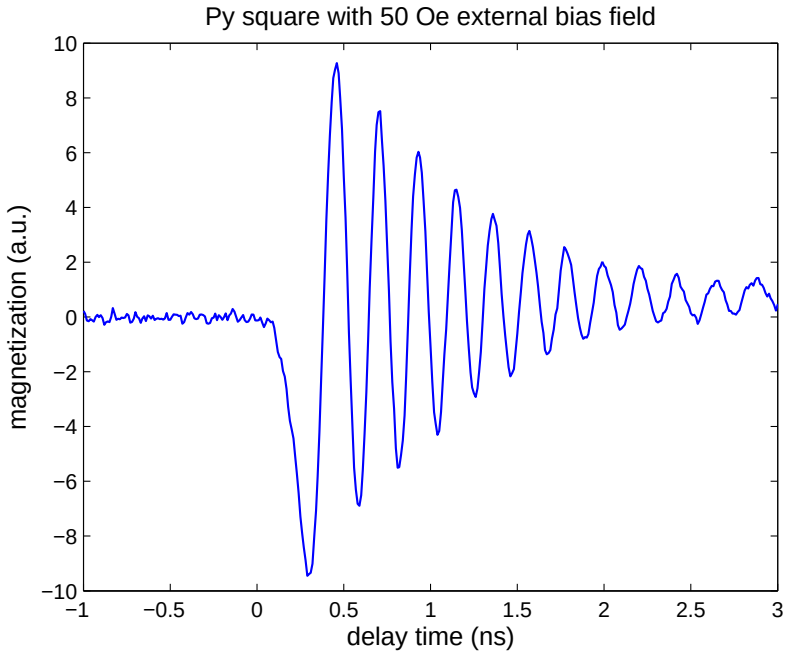

Figure 5.10: Py square magnetization dynamics raw data.

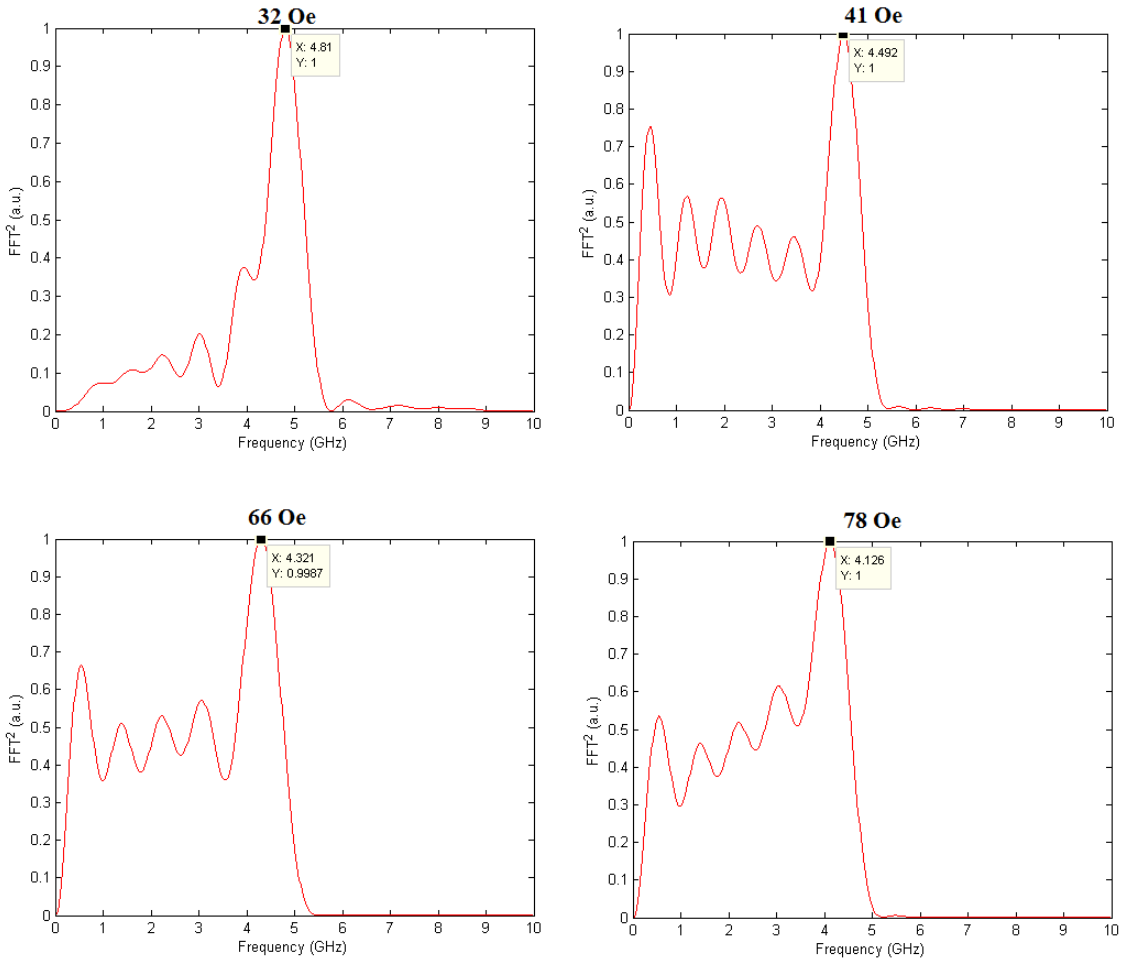

Figure 5.11: Py square top domain FFT results.

After the temporal magnetization from the Py square in Fig. 5.10 is detected, we pick the regular damped-oscillation range after pump excitation for FFT. For example, in Fig. 5.10, we pick the time range 0.25-3 ns for FFT.

The relation between the magnetic precession frequencies and the external bias field strength can be extracted from the FFT results shown in Fig. 5.11 and Fig. 5.12.

Fig. 5.13 shows that the precession frequencies in the top and bottom domains both decrease with the increasing in-plane magnetic bias field.

Simulation and experimental results of the precession frequencies show the same trend for the top and bottom domain, although the quantitative parameters can not

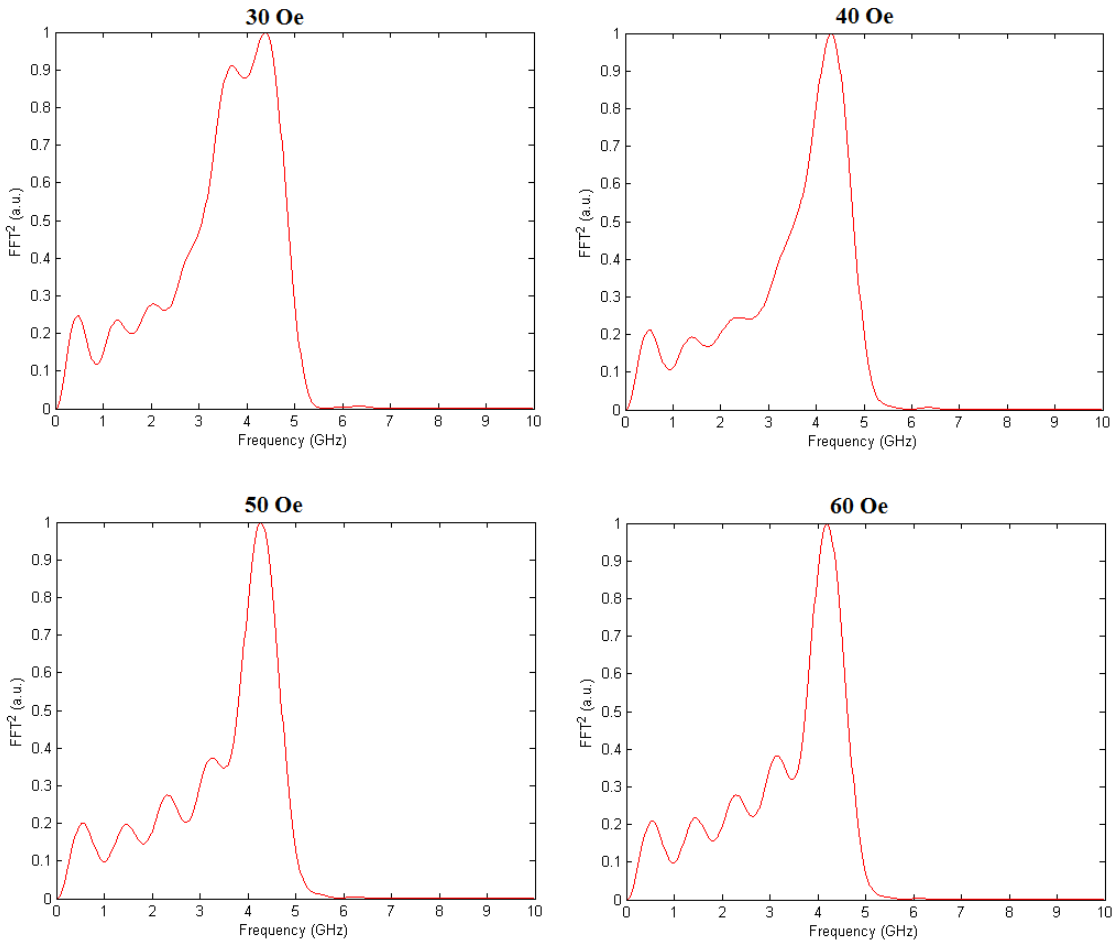

Figure 5.12: Py square bottom domain FFT results.

be directly compared. In the low bias field situation, the precession frequency in the top domain is larger than that in the bottom domain and decreases rapidly with increasing bias field strength. Yet when the bias field is larger than some certain value, the precession frequency in both domain saturates into the same decreasing trend.

Additionally, the precession dynamics in the left and right domain are observed in the simulation (See Fig. 5.14). Plotting with the same frequency scale as the top and bottom domain, we find that the precession frequencies in the left and right domain share the same trend and they are independent of the external bias field increase. The little fluctuation of the frequency in the Fig. 5.15 comes from the FFT uncertainty.

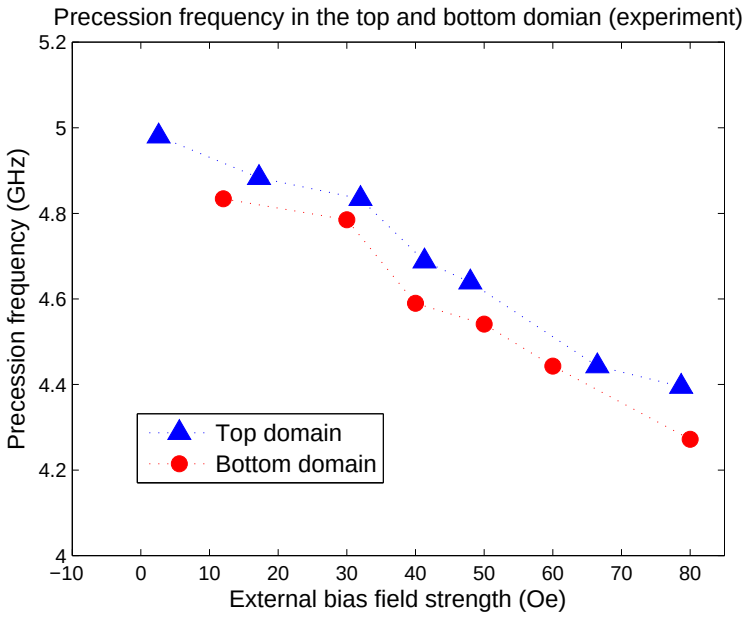

Figure 5.13: Top and bottom domain precession frequencies from the experiment data.

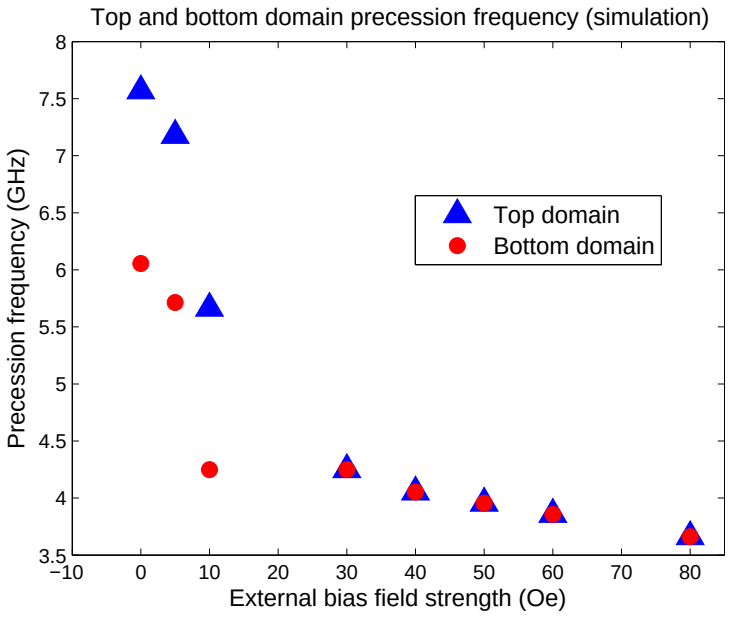

Figure 5.14: Top and bottom domain precession frequencies from the simulation data.

5.2.3 Effective damping constant

The raw data of the magnetization dynamics is fitted with a damped-oscillation function. This curve fitting gives us the information about the precession frequency

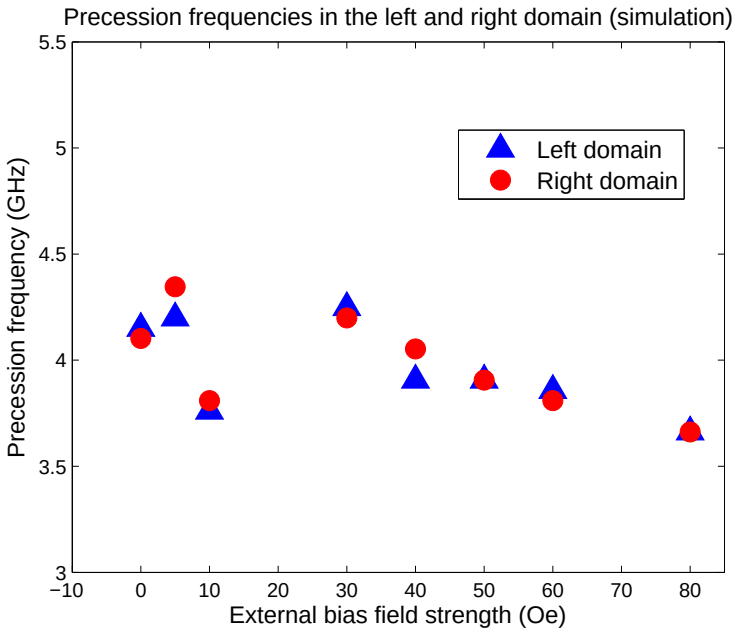

Figure 5.15: Left and right domain precession frequencies from the simulation data.

and effective damping constant, as shown in Fig. 5.16.

By FFT and curve fitting, we get the precession frequencies for each top and bottom domain. By plotting these two frequency values together, we check the reliability of curving fitting. The error bars come from the parameter range in the curving fitting.

The little difference between FFT frequency and the curve fitting frequency results from the step size and accuracy of the FFT program.

Besides, we also obtain the information about relaxation time τ and the effective damping constant $\alpha_{eff} = 1/2\pi f\tau$. In Fig. 5.19, the damping constants in the top and bottom domains decrease with increasing bias field at different rates just like precession frequency.

In my experiment, the minimum value of effective damping constant is about 0.018 in the top domain with the 80 Oe bias field. This puts an upper limit on the value of the Gilbert damping constant. As mentioned in reference [24], the Gilbert damping constant of a 12 nm Py film detected by MOKE is around 0.008, which is consistent with my experiment result.

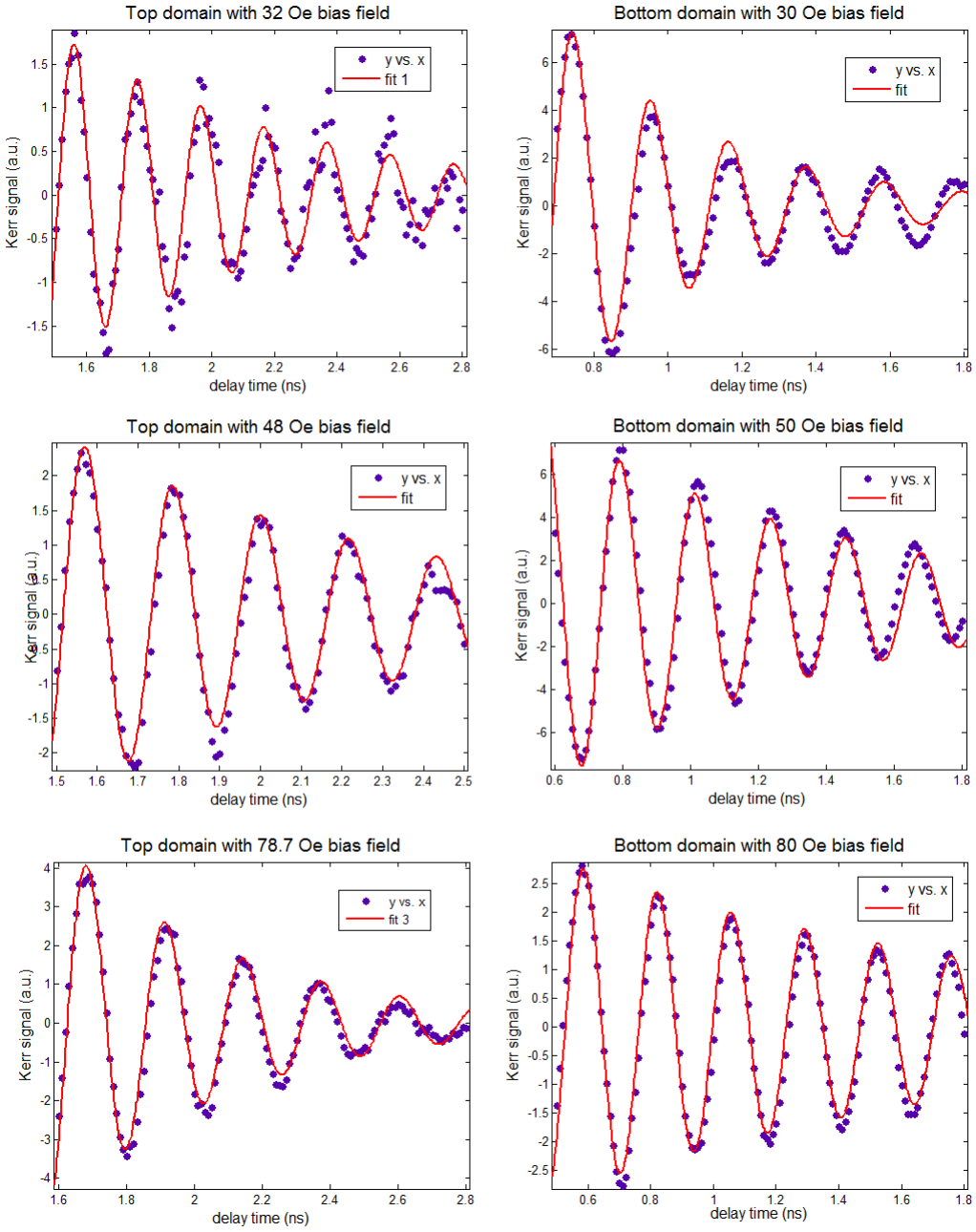

Figure 5.16: Top and bottom domain curve fit results.

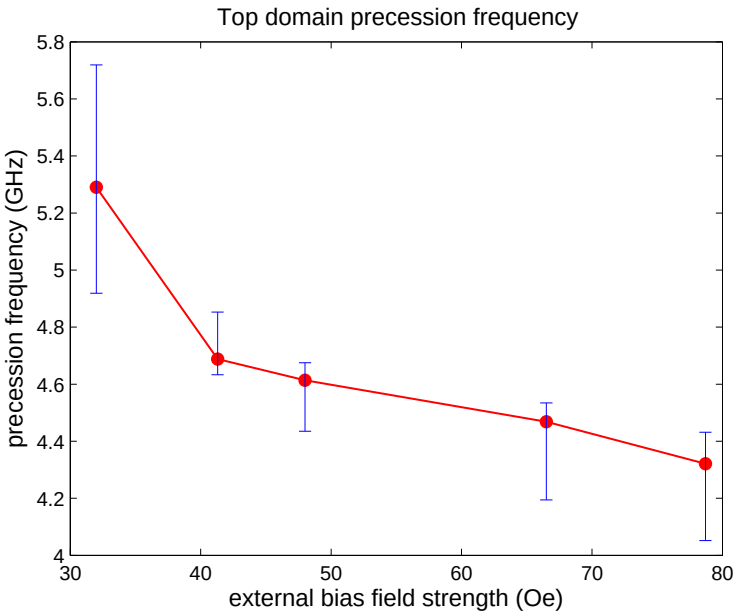

Figure 5.17: Top domain precession frequency. Red dots are the FFT results, red line is eye guide of FFT results and blue error bars are the precession frequency range from the curve fitting.

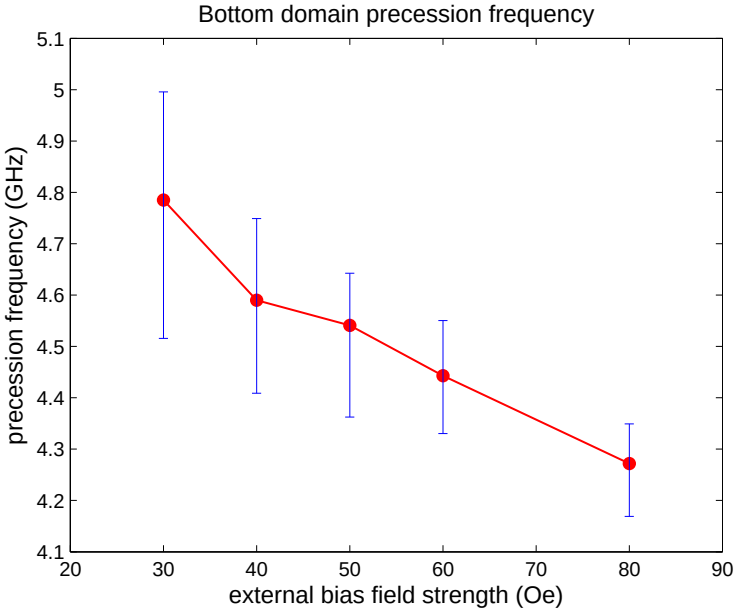

Figure 5.18: Bottom domain precession frequency. Red dots are the FFT results, red line is eye guide of FFT results and blue error bars are the precession frequency range from the curve fitting.

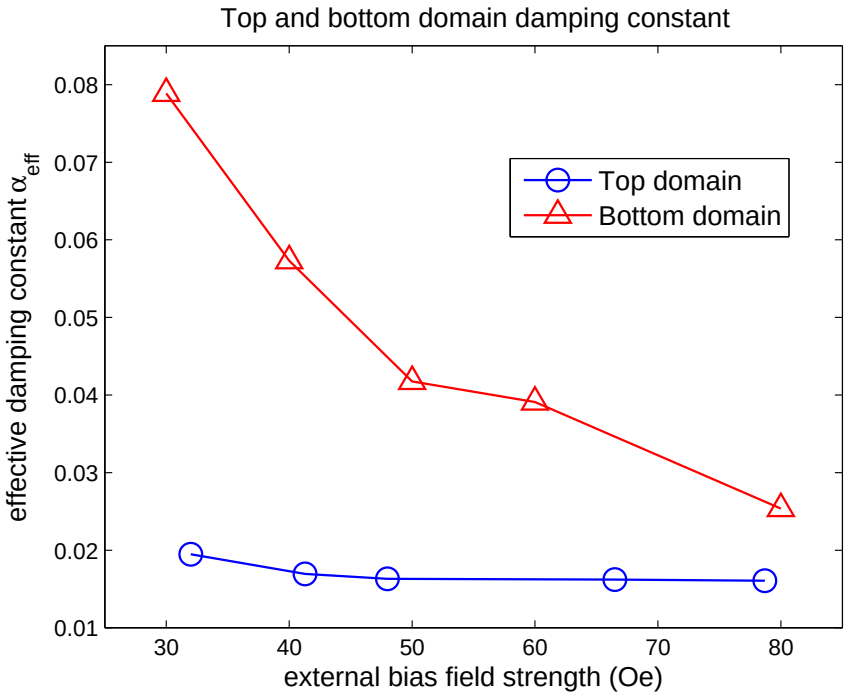

Figure 5.19: Effective damping constants in the Py square.

5.3 Fe-Pt alloy

Generally, Fe-Pt alloys have two phases depending on the growth condition, but only the Fe-Pt alloy with $L1_0$ phase is ferromagnetic (See Fig. 5.20).

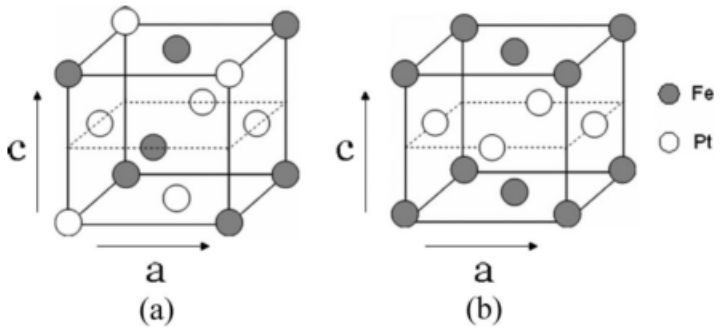

Figure 5.20: The two crystal phases of FePt. (a) A_1 phase, also called fcc phase with $a = c$. (b) $L1_0$ phase, also called face centered tetragonal phase, $a \neq c$. From [25]
.

In the phase $L1_0$, FePt forms a thermodynamically stable superlattice structure. This gives the high perpendicular anisotropy, which can be applied in ultrahigh density memory devices. As a promising material for the new generation memory device, we are interested in its dynamic properties such as resonance frequency and damping constant.

5.3.1 Hysteresis measurement

As shown before in Chapter 3, the optical pump beam has a thermal demagnetizing effect on the sample. Theoretically, when the pump and probe pulses are overlapped in time, the small area in the sample will be heated past the Curie temperature and lose its magnetization. This kind of demagnetization effect can be shown in the hysteresis measurement (See Fig.5.21).

Obviously, the saturation magnetization is depressed with pump heating, compared to equilibrium, and gradually recovers.

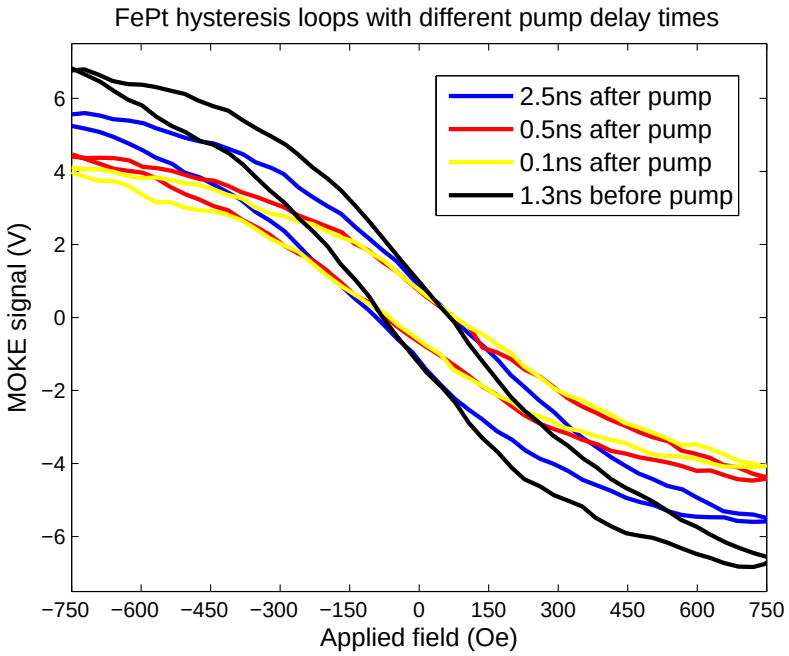

Figure 5.21: FePt hysteresis measurement with different pump delay times.

5.3.2 All optical pump-probe technique

Using the stroboscopic pump-porbe technique, we can get the temporal dynamic information showing that the magnetization disappears and recovers with precession after the pump pulse. Typical results are shown in Fig. 5.22.

For the Fe-Pt alloy, the demagnetization process happens within several picoseconds. And the demagnetization amplitude is around 7%, which is consistent with the results given in the reference [26]. Then, the magnetization precesses with GHz frequency. We applied FFT to several groups of dynamics data, and found that the major frequency peak is around 1.69 GHz.

5.4 $Co_{60}Fe_{20}B_{20}$

$Co_{60}Fe_{20}B_{20}$/MgO is very promising for the application of magnetic tunnel junctions (MTJs) with a perpendicular magnetic easy axis. This material show a high tunnel magnetoresistance ratio over 120%, high thermal stability at the dimension as low as 4 nm diameter. [27] However, this high perpendicular-anisotropy material needs a reasonable damping parameter and switching current magnitude to make it applica-

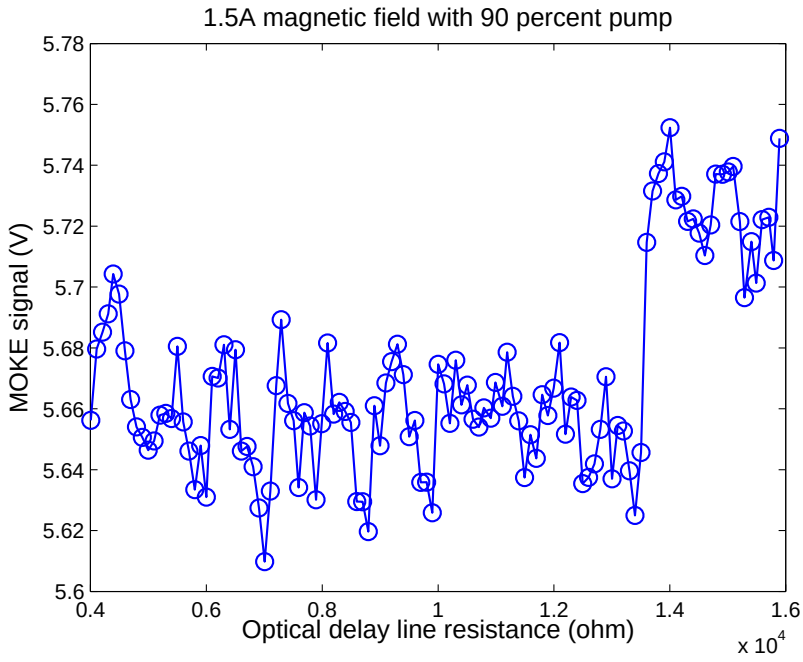

Figure 5.22: FePt Temporal dynamics

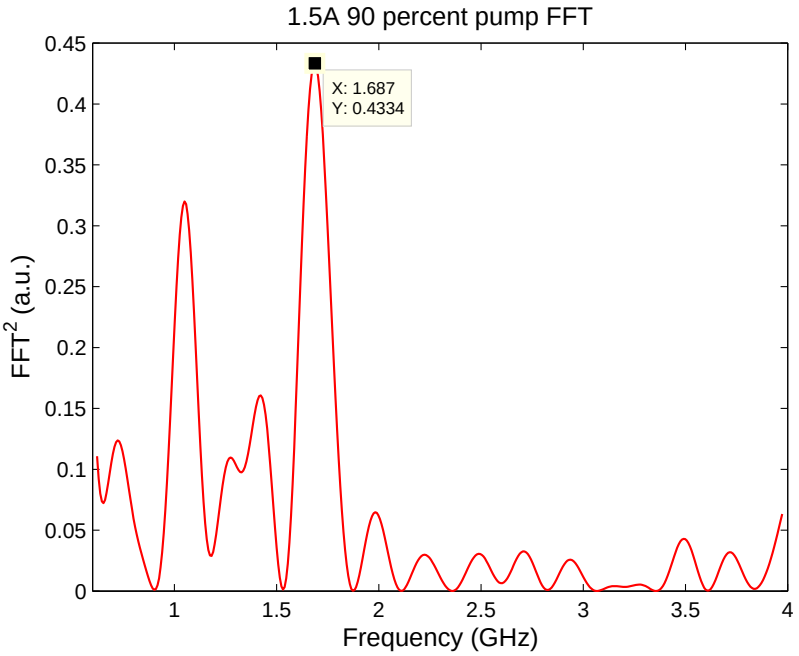

Figure 5.23: Fourier transformation graph of FePt film

ble. Therefore, I explored the temporal magnetization properties of $Co_{60}Fe_{20}B_{20}$/MgO in microscopic disk elements.

5.4.1 Fabrication and deposition

I used the electron beam lithography (EBL) to fabricate the disc pattern (ex. 5.25) and sent these wafers to University of Alabama for sputter deposition of the materials. The sample deposition sequence has been shown in 5.24.

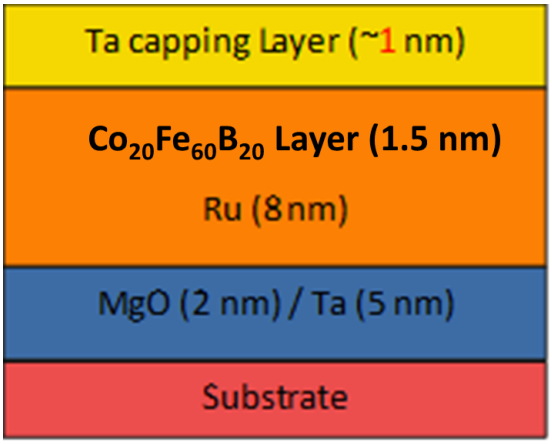

Figure 5.24: $Co_{60}Fe_{20}B_{20}$/MgO sample deposition sequence.

5.4.2 Temporal data

Using the gold coil to excite the magnetization out-of-plane or in-plane, I employed the pump-probe technique to detect the temporal magnetization process in $Co_{60}Fe_{20}B_{20}$/MgO bilayer discs.

Unfortunately, I could only get the rough excitation information but not the clear damping shape. Typical raw data looks like as Fig. 5.26.

Obviously, the ratio of signal and noise is quite small. To amplify the signal, I have tried the following improvement methods: (1) change the excitation polarity and external bias field configuration, (2) finely tune the working distance from the objective lens to the sample surface, (3) both in-plane and out-of-plane excitation, and (4) probed different domain regions on the single disk sample.

Fig. 5.27 shows the maximum excitation peak amplitude we could get from this sample. The excitation feature is obvious and accurately repeatable in the time. Yet

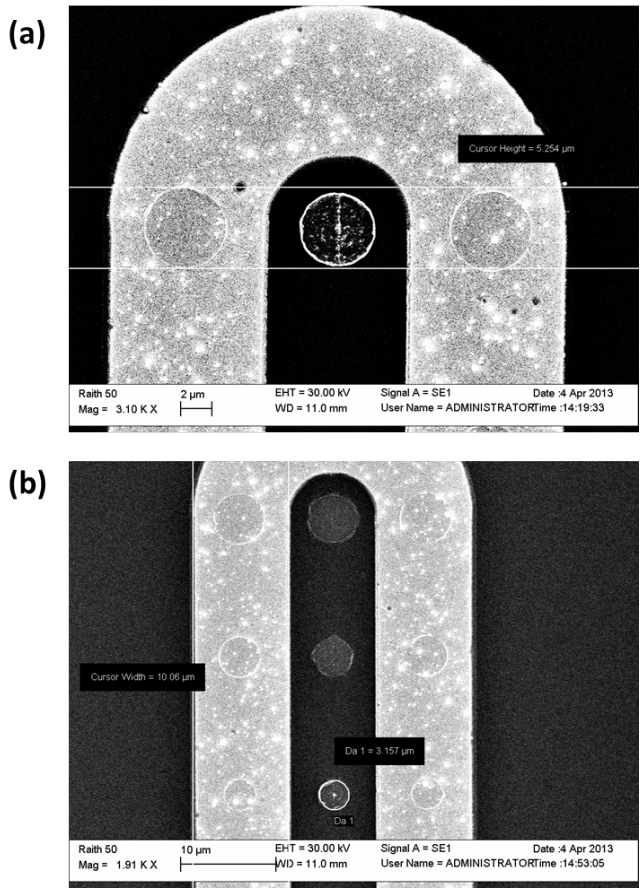

Figure 5.25: Scanning electron microscopy (SEM) picture of the sample disks. (a) 10 μm-diameter disk (b) disk array with different sizes

the precession frequency and exponential decay features are too noisy for the data processing.

5.4.3 Contamination EDX analysis

Here I summarize several reasons for that I could not improve the signal quality more.

First of all, the thickness of the sample film, 1.5nm, is very thin compared to the penetration depth of the laser. Naturally, the magnetic signal will not be as strong as the bulk material. Yet our research interest lie in the ultrathin-film and structures below μm dimension.

The most noise in my experiment comes from the contamination mixed in the gold coil as seen in Fig. 5.25. These random and numerous dots in the SEM picture 5.28

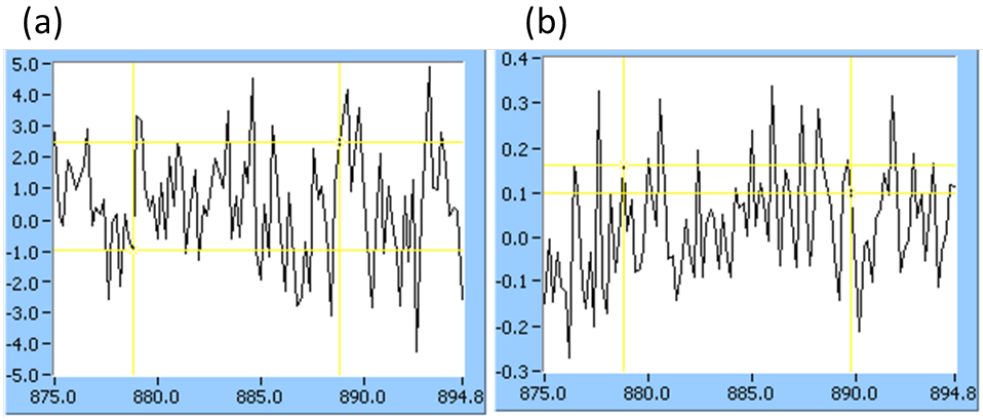

Figure 5.26: Raw data of $Co_{60}Fe_{20}B_{20}$-MgO sample in the Labview program. (a) positive polarity excitation pulse (b) negative polarity excitation pulse

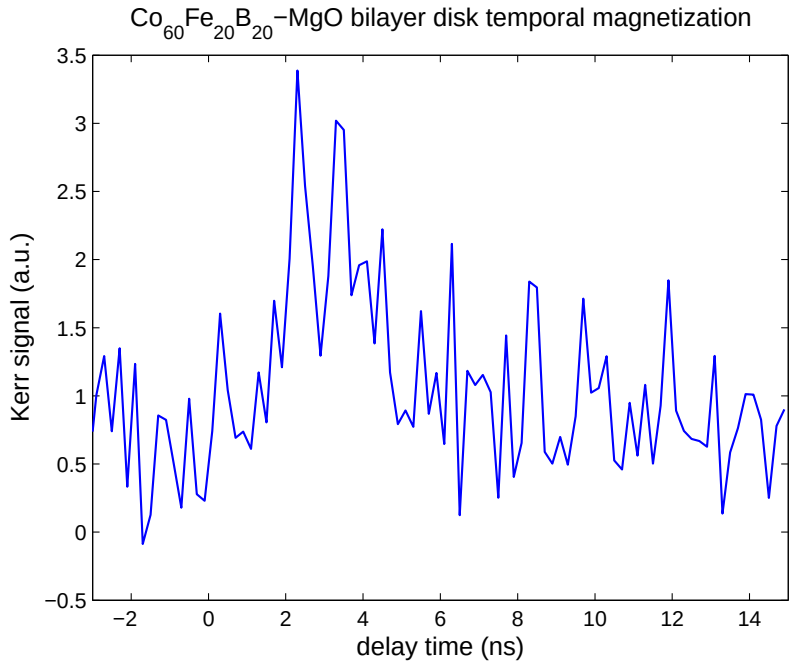

Figure 5.27: Temporal magnetization of the 10 μm diameter $Co_{60}Fe_{20}B_{20}$/MgO disc.

are around 100 nm diameter. And they can not be totally washed by acetone or IPA, even with ultrasonic cleaning. Several black holes close to the center in Fig. 5.28 are the silicon wafter exposed after contamination particles are removed by sonication.

To determine the composition of these contamination dots, we use energy-dispersive X-ray spectroscopy (EDX) for the chemical analysis. The energy of X-rays are char-

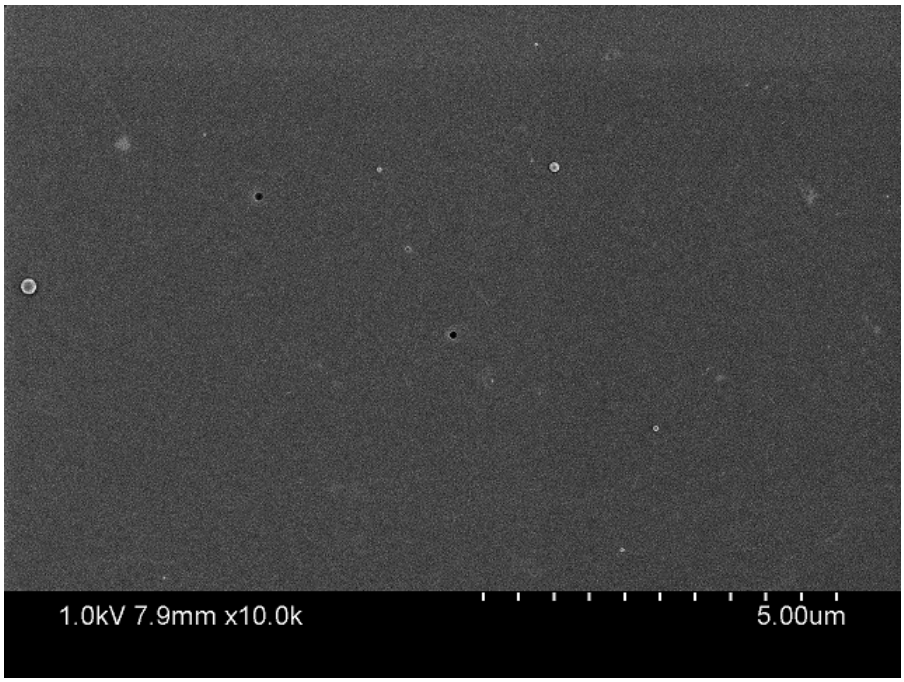

Figure 5.28: Si wafer deposited with contaminated Au.

acteristic of the difference in energy between the two shells of specific element. The spectrum shows that there are no carbon or other metal particles. So the contamination particles do not come from the crucible or targets of the evaporation system. They are pure gold.

The reason for the random-size big dots is that the gold target is almost used up and the electron beam is too powerful for the heating. So the gold target went through a uneven solid-liquid-gas mixed phase. After these, we have refilled the Au target and lower the electron beam intensity and the deposition rate, which improves the film quality. Yet these particles formation still happened in deposition process. It may affect the nanometer structure conductivity and optical properties, especially for those structures with dimension below 500 nm.

Chapter 6

Analysis and conclusion

6.1 Analysis

As shown in the previous chapter, we find that in the permalloy square sample the precession frequency decreases with the external field strength while the effective damping constant in the top and bottom domain shows different trends.

6.1.1 Bias field orientation

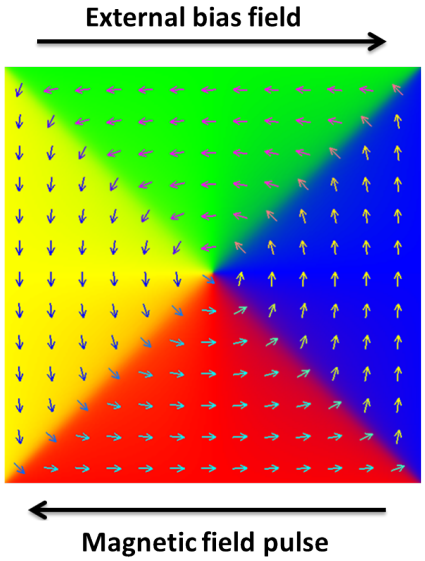

Figure 6.1: Landau-vortex configuration and external bias field orientation.

As shown in the schematic Fig.6.1, the external bias field is applied in the plane of the sample. The magnetic field pulse is antiparallel with the bias field. Considering the anisotropy energy in the Landau-vortex configuration, the Kittel equation 5.1 can modified as

$$f = \frac{\mu_0 \gamma}{2\pi} \sqrt{(H_{pulse} - H_{bias} + H_{an} + M_s)(H_{pulse} - H_{bias} + H_{an})}. \tag{6.1}$$

Here H_{pulse} is the magnetic field pulse, H_{bias} is the external magnetic bias field and H_{an} is the effective field from the anisotropy energy inside the sample. The anisotropic field effect is small compared with the magnetic pulse and bias field. Therefore, when we increase the bias field strength, the value of $H_{pulse} - H_{bias}$ gets smaller, which explains the decreasing trend of the precession frequency.

According to [28], the effective anisotropy vector field H_{an} can be written as

$$H_{an} = \frac{H_k(\mathbf{M})}{4}(2\sin 2\theta \sin\theta + \cos 2\theta \cos\theta), \tag{6.2}$$

with $H_k(\mathbf{M})$ is the anisotropy coefficient depending on the magnetization $\mathbf{M}$, and θ is the angle between the magnetization and the effective magnetic field, $H_{pulse} - H_{bias}$ in this case. For the top domain, magnetization and magnetic field has the parallel configuration, ie. $\theta = 0$ and $H_{an} = H_k/4$. Then the antiparallel configuration in the bottom domain leads to $\theta = 180$ and $H_{an} = -H_k/4$. The sign of the anisotropic effective field term results in a higher precession frequency in the top domain than in the bottom domain. Large bias field saturates the uniformity of the magnetization and finally give rise to the same precession frequency trend in both the top and bottom domain.

The vortex configuration also explains the simulation result of precession frequencies in the left and right domain. As shown in Fig. 5.15, the precession frequencies in the left and right domain show the same trend with the increasing bias field. Magnetization directions in the left and right domain are both perpendicular with the bias field orientation, which leads to equivalent precession motion in these two domains.

6.1.2 Damping constants

The damping constants in the bottom domain of the Py square decreases with the increasing bias field while the damping constants in the top domain show no significant change (See Fig. 5.19). In the top domain, the parallel configuration leads to a small

angle excitation, in which the magnetization precesses in a uniform fashion. With the antiparallel configuration in the bottom domain, the magnetization undergoes a large-angle excitation, and this leads to the large value of damping constants due to nonuniform precessional motion of **M**. Yet with increasing external bias field, the magnetization in the square sample saturates uniformly at some large bias field. In this single domain case, the damping dynamics in the top and bottom quadrant position is the same. As shown in Fig. 5.19, the damping constants in the top and bottom domain tends to saturate at the same value with the increasing bias field. The analytic mathematic relation between damping constants and bias field strength has not been explored yet.

6.2 Conclusion

In this thesis, I introduced the theory of micromagnetism and the critical Landau-Lifshitz-Gilbert equation. Then I explored the physical meaning of the Gilbert damping term in the Chapter 3. The effective damping parameter includes several mechanisms. In Chapter 4 I summarized the principle of magneto-optic Kerr effect and described the experimental setup in detail. After testing the reliability of the setup with a reference sample (YIG), I measured the temporal magnetization process of Py square samples. The data is analyzed to extract the precession frequency and the damping parameter.

The domain configuration in the Py square is confirmed by both micromagnetic simulation and experimental hysteresis measurement. Using the FFT in Matlab, I find out the precession frequency dependence on the bias field strength. Besides, the values of effective damping constant are obtained by curve fitting analysis. The minimum effective damping constant in my experimental measurement, 0.018 with 80 Oe bias field, sets up an upper boundary for the estimation of Gilbert damping constant. The high effective damping constants measured at small bias field are attributed to the contribution of the indirect damping caused by the excitation of spin waves.

6.3 Future work

Some instrumental improvements for future work are suggested below.

- All optical pump-probe TR-MOKE

    1. Increase the pump heating absorption rate: By add some other non-magnetic material membrane or particle arrays, we could increase the laser heating absorption rate and improve the demagnetization effect.
    2. Objective lens magnitude: In my experiment, we use the 80X microscopic lens. Later, we could try higher-magnitude lens, such as 100X immersion oil lens with short focal lens. This would require us to use thinner glass substrates in the sample preparation.
    3. Delay line time resolution: We could use the digital multi-meter to read the delay time resistance. This floating decimal reading could control the resistance fluctuation within 1 ohm. With this setup, time step is around 0.5 ps second.

- Electromagnet design

    1. External bias field orientation: We could design a rotatable stand for the electromagnet. For the perpendicular-anisotropy magnetic material measurement, we excite the sample magnetization out-of-plane. Ideally, a 90-degree rotatable electromagnet would be beneficial.
    2. Field strength: With the electromagnet and power supply we have by now, the highest magnetic field strength is around 2000 Oe. According to the reference, to study the hard magnetic material such as FePt, we need strong external field. That may be realizable with the rare-earth permanent magnet in the Halbach array configuration.

Appendix A

Microcoil magnetic field pulse calculation

A ring-shaped microcoil is fabricated on the sample in order to give ultrafast magnetic field pulse. Here is a calculation for magnetic field magnitude and gradient distribution within detection area inside the microcoil.

The gold coil can be approximated by concentric rings of width $w = 10\mu m$, thickness $d = 100nm$, inner radius $a = 1\mu m$, external radius $b = 11\mu m$ in the xy plane ($d \ll$ other dimensions), and we can ignore its thickness for approximation.

Considering a current evenly distributed in the coil, the surface current density J is given by

$$J = \frac{I}{\pi(b^2 - a^2)}. \tag{A.1}$$

Here, pulse voltage output is 45 volts, and we measure the resistance of the coil circuit to be 50Ω, so I = 0.9 A.

With the Biot-Savart law,

$$\vec{B} = \frac{\mu_0}{4\pi} \int \frac{Id\vec{l} \times \vec{r}}{\mid \vec{r} \mid^3}, \tag{A.2}$$

we can calculate the current-induced magnetic field inside the circular coil. We use the polar coordinates for convenience and choose the center of the circles as the origin.

Now, we can give the position of any point A inside coil as (m, n), any point B on the coil as $(rcos\theta, rsin\theta)$, the vector from A to B as r', $r' = (rcos\theta - m, rsin\theta - n)$,

and the unit vector $d\vec{l}$, $\hat{n} = (-sin\theta, cos\theta)$.

The double integral over coil surface reads

$$\vec{B} = \frac{\mu_0}{4\pi} \int_a^b dr \int_0^{2\pi} J \cdot \frac{\vec{r} \cdot \hat{n} \times \vec{r'}}{\mid \vec{r'} \mid^3} d\theta. \tag{A.3}$$

For the integral over theta, we use the trapezoid numerical integral in Matlab, and manually set step size and integrate over radius r. And save magnetic field result B for every point inside coil into the variable Matrix $B(i, j)$ and plot.

The Matlab code is listed below:

```
% Give number of calculation steps n: then coil center area is divided by
% n*n mangetic field value is input in matrix B

global a b t X Y Z m n l
t=30;
B= zeros(t);
H1= zeros(t);
H2= zeros(t);
H3= zeros(t);
%radius integral step size l
l=0.05;

%inner radius a 1um, outer radius b 11 um
a = 1;
b = 11;


for i=1:t
   for j=1:t
       for r=1:l:6

       m= -1+(2/t)*(i-1);
       n= -1+(2/t)*(j-1);

       X = 0:pi/100:2*pi; % not a whole ring, has 45 degree opening
       Y = [r-n.*sin(X)-m.*cos(X)]./[(r.^2 + m.^2+ n.^2 - 2*r.*(m.*cos(X)+n.*sin(X)↩
           )).^(3/2)];
       Z = trapz(X,Y);
       B(i,j)=Z.*r.*l*0.0228*pi/(b-a);
       % B has unit of Gauss
       H1(i,j)= B(i,j)*10^6;
       % H has unit of oesterd
       end

   end
```

```
end

for i = 1:t
    for j = 1:t
       for r = 1:100

       m= -1+(2/t)*(i-1);
       n= -1+(2/t)*(j-1);

       y= -9- 0.1*(r-1);

       X = 0.5:0.1:10;
       Y = (X-m)./[((X-m).^2+(y-n).^2).^(3/2)];
       T = (X+m)./[((-X-m).^2+(y-n).^2).^(3/2)];
       Z = trapz(X,Y)+ trapz(X,T);

       H2(i,j)=H2(i,j)+ Z.*0.9*0.1*10^3;
       % H has unit of oesterd

       end
    end
end

H3=H1-H2;

surf(H3);
colormap(jet)
```

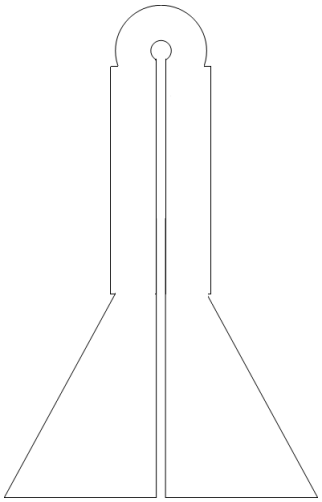

Figure A.1: Ring shape coil.

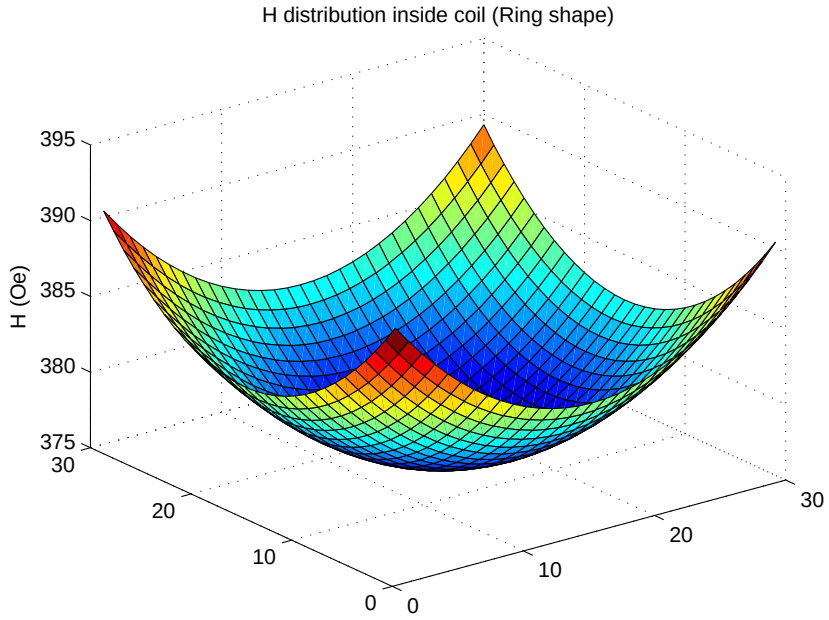

Figure A.2: Magnetic field intensity B_z distribution for the ring-shaped coil.

Bibliography

[1] a V Khvalkovskiy, D Apalkov, S Watts, R Chepulskii, R S Beach, a Ong, X Tang, a Driskill-Smith, W H Butler, P B Visscher, D Lottis, E Chen, V Nikitin, and M Krounbi. Erratum: Basic principles of STT-MRAM cell operation in memory arrays. *Journal of Physics D: Applied Physics*, 46(13):139601, April 2013.

[2] M D'Aquino. Nonlinear magnetization dynamics in thin-films and nanoparticles. (December), 2004.

[3] Mohamad T Krounbi, S Watts, D Apalkov, X Tang, K Moon, V Nikitin, A Ong, V Nikitin, and E Chen. Status and Challenges for Non-Volatile Spin-Transfer Torque RAM (STT-RAM). pages 1–28, 2010.

[4] L Landau and E Lifshitz. On the theory of the dispersion of magnetic permeability in ferromagnetic bodies. *Phys Z Sowjetunion*, 8(14):14–22, 1935.

[5] T L Gilbert. A phenomenological theory of damping in ferromagnetic materials, 2004.

[6] Jakub Lengiewicz and Stanisaw Stupkiewicz. Continuum framework for finite element modelling of finite wear. *Computer Methods in Applied Mechanics and Engineering*, 205-208:178–188, January 2012. ISSN 00457825.

[7] P Podio-Guidugli. On dissipation mechanisms in micromagnetics. *The European Physical Journal B-Condensed Matter ...*, 17:1–19, 2001.

[8] Ryoichi Kikuchi. On the Minimum of Magnetization Reversal Time. *Journal of Applied Physics*, 27(11):1352, 1956.

[9] Georg Woltersdorf. Spin-pumping and two-magnon scattering in magnetic multilayers. (August), 2004.

[10] H Suhl. Theory of the magnetic damping constant. *Magnetics, IEEE Transactions on*, 1998.

[11] B. Heinrich, D. Fraitov, and V. Kambersk. The influence of s-d exchange on relaxation of magnons in metals. *physica status solidi (b)*, 23(2):501–507, 1967.

[12] Xinguo Ren, Patrick Rinke, Christian Joas, and Matthias Scheffler. Random-phase approximation and its applications in computational chemistry and materials science. 1953.

[13] M Djordjević Kaufmann. Magnetization dynamics in all-optical pump-probe experiments: spin-wave modes and spin-current damping. 2006.

[14] V Kamberský. On the Landau-Lifshitz relaxation in ferromagnetic metals. *Canadian Journal of Physics*, 1970.

[15] D. Steiauf and M. Fähnle. Damping of spin dynamics in nanostructures: An ab initio study. *Physical Review B*, 72(6):064450, August 2005. ISSN 1098-0121.

[16] Shigemi Mizukami, Takahide Kubota, Xianmin Zhang, Hiroshi Naganuma, Mikihiko Oogane, Yasuo Ando, and Terunobu Miyazaki. Influence of pt doping on gilbert damping in permalloy films and comparison with the perpendicularly magnetized alloy films. *Japanese Journal of Applied Physics*, 50(10):103003, 2011.

[17] R. Yilgin, M. Oogane, and S. Yakata. Intrinsic Gilbert damping constant in Co 2 MnAl Heusler alloy films. *... IEEE Transactions on*, 41(10):2799–2801, October 2005.

[18] C Lu, A W Czanderna, and Alan Townshend. Applications of piezoelectric quartz crystal microbalances. *Analytica Chimica Acta*, 199(0):279, 1987.

[19] P.M. Oppeneer. volume 13 of *Handbook of Magnetic Materials*. 2001.

[20] Dana Elena. *Magnetization Dynamics in Magnetic Nanostructures*. PhD thesis, Université Joseph Fourier, 2004.

[21] M van Kampen. Ultrafast spin dynamics. *Technische Universteit Eindhoven*, 2003.

[22] S. Mizukami, S. Iihama, N. Inami, T. Hiratsuka, G. Kim, H. Naganuma, M. Oogane, and Y. Ando. Fast magnetization precession observed in L1[sub 0]-FePt epitaxial thin film. *Applied Physics Letters*, 98(5):052501, 2011.

[23] Controlled enhancement of spin-current emission by three-magnon splitting. *Nature materials*, 10(9):660–4, September 2011. ISSN 1476-1122.

[24] Jakob Walowski. Non-local/local gilbert damping in nickel and permalloy thin films. 2007.

[25] By Jian-ping Wang. FePt Magnetic Nanoparticles and Their Assembly for Future Magnetic Media. *Proceedings of the IEEE*, 96(11):1847–1863, November 2008.

[26] Jiaqi Zhao, Boyin Cui, Zongzhi Zhang, B. Ma, and Q.Y. Jin. Ultrafast heating effect on transient magnetic properties of L10-FePt thin films with perpendicular anisotropy. *Thin Solid Films*, 518(10):2830–2833, March 2010.

[27] S Ikeda, K Miura, H Yamamoto, K Mizunuma, H D Gan, M Endo, S Kanai, J Hayakawa, F Matsukura, and H Ohno. A perpendicular-anisotropy CoFeB-MgO magnetic tunnel junction. *Nature materials*, 9(9):721–4, September 2010. ISSN 1476-1122.

[28] H Fujiwara and T Zhao. Effective magnetic anisotropy vector field. *Journal of Magnetism and Magnetic Materials*, 218:129–131, 2000.